J. Fluid Mech. (1997), *vol.* 352, *pp.* 27–64. Printed in the United Kingdom

Kidney and anti-kidney vortices in crossflow jets

By B. A. HAVEN† AND M. KUROSAKA

Department of Aeronautics and Astronautics, University of Washington, Seattle, WA 98195-2400, USA

(Received 10 June 1996 and in revised form 7 July 1997)

Water tunnel experiments were conducted to examine the effect of hole exit geometry on the near-field characteristics of crossflow jets. Hole shapes investigated were round, elliptical, square, and rectangular, all having the same cross-sectional area. Laser-induced fluorescence (LIF) and particle image velocimetry (PIV) were used.

The vorticity around the circumference of the jet was tracked to identify its relative contributions to the nascent streamwise vortices, which evolve eventually into kidney vortices downstream. The distinction between sidewall vorticity and that from the leading and trailing edges, though blurred for a round hole, became clear for a square or a rectangular hole. The choice of non-circular holes also made it possible to reveal the unexpected double-decked structures of streamwise vortices and link them to the vorticity generated along the wall of the hole.

The lowermost vortex pair of the double-decked structures, located beneath the jet, is what we call a 'steady' vortex pair. This pair is always present and has the same sense of rotation as the kidney vortices. The origin of these lower-deck vortices is the hole sidewall boundary layer: as the jet emanates from the hole, the crossflow forces the sidewall boundary layer to roll up into nascent kidney vortices. Here, hole width sets the lateral separation of these steady sidewall vortices.

The vortices comprising the upper deck ride intermittently over the top of the 'steady' lower pair. The sense of rotation of these upper-deck vortices depends on hole geometry and can be the same as, or opposite to, the lower pair. The origin of the upper deck is the hole leading-edge boundary layer. This vorticity, initially aligned transverse to the crossflow direction, is realigned by the entrainment of crossflow momentum and thus induces a streamwise component of vorticity. Depending on hole geometry, this induced streamwise vorticity can be opposite to the lower-deck vortex pair. The opposing pair, called the 'anti-kidney' pair, competes with the nascent kidney-vortices and affects the jet lift-off. The hole trailing-edge boundary layer can likewise be turned toward the streamwise direction. In this case, the turning is caused by the strong reverse flow just downstream of the jet.

In the present range of parameters, all hole boundary layer vorticity, regardless of its origin along the hole circumference, is found to influence the kidney vortices downstream.

1. Introduction

Crossflow jets have been used in many technological applications: film cooling for turbines and combustors, fuel injection for burners, vectored thrust and thrust

† Present address: Department of Aeronautics, US Air Force Academy, Colorado Springs, CO 80840-6222 USA.

reversers for propulsive systems, pollutants emitted from chimneys, and effluent discharged from a pipe into rivers. Depending on the specific applications, the objectives are naturally different. For an application such as smokestack discharge, the vertical rise of the plume and diffusion into atmosphere are of main concern. For film cooling, the motivation for the present paper, however, the attachment of the jet to the wall is crucial.

In film cooling used in gas turbines, coolant is introduced to the hot gas stream of the turbine section as crossflow jets. The coolant forms a film layer over the turbine walls, protecting the surface from direct exposure to the hot gas stream. As with any crossflow jet, a pair of counter-rotating vortices is formed as the jet interacts with the oncoming crossflow. These vortices, often referred to as kidney-shaped vortices, have a sense of rotation that promotes both the jet lift-off and entrainment of the crossflow towards the wall; thus they can seriously degrade the effectiveness of the film layer in protecting the surface (e.g. Haven & Kurosaka 1996).

The need for improved cooling performance has lead to the advent of 'shaped' holes, those with non-circular exit cross-section. Efforts to improve systematically shaped holes are, unfortunately, thwarted by the countless parameters needed to define the non-circular geometry and by the basic lack of fluid dynamical understanding of why shaped holes work.

It is, however, conceivable that the very departure from the round hole could somehow change the kidney vortices, which, in turn, improves the ability of the jet to adhere to the wall. To confirm this supposition, the paper aims to establish the relationship between the kidney-vortex structures and basic non-circular hole geometries such as a square, rectangle and ellipse. To simplify the matter further, we will focus on a single jet injected normally into the crossflow. Despite their simple configurations, there is a dearth of studies on the kidney vortices for these geometries, past research having been limited primarily to round holes.

Historically, Scorer (1958) appears to be among the first who called attention to the presence of counter-rotating vortices in a crosswind. From a simple argument for upward momentum, he deduced a formula for jet rise. He also proposed that the counter-rotating vortices were formed from the roll-up of the vorticity at the sides of the round orifice only; the vortices at the leading and trailing edges of the round orifice are considered to annul each other.

At present, literature that addresses the kidney vortices abounds. The following is just a partial list of recent related papers (for a more complete list, see Haven 1996): Andreopoulos (1982), Andreopoulos & Rodi (1984), Broadwell & Breidenthal (1984), Sykes, Lewellen & Parker (1986), Fric (1990), Fric & Roshko (1994), and Kelso, Lim & Perry (1996).

On the question of the origin of the kidney pair for the round hole, recent investigations by Fric (1990) and Fric & Roshko (1994) clarified the role of wake vortices in entraining the crossflow boundary layer into the rear side of the jet, while Kelso *et al.* (1996) investigated the contribution of the wake vortices to the downstream kidney vortices.

Kidney vortices are, however, known to form upstream of the wake region while the jet is still over the hole (e.g. Crabb, Durao & Whitelaw 1981); therefore, kidney vortices must have their origin somewhere in the jet pipe boundary layer. Sykes *et al.* (1986) and others attribute this origin to essentially the same mechanism as that proposed by Scorer (1958): the vorticity initially on the sides of the round hole. The question of what happens to the remaining pipe boundary layer vorticities, such as those at the leading and trailing edges which are initially aligned transverse to the

flow, is either left unaddressed or explained by appealing to the vorticity cancellation process originally proposed by Scorer (1958).

This question of what other vorticity from the pipe boundary layer contributes to the kidney vortices is pertinent since any vorticity can be turned in the flow. Such turning can, in fact, be highly important, especially at the leading edge of the jet, where entrainment of the crossflow momentum into the jet can deform and realign the transverse vortex filaments within the boundary layer. Likewise, at the trailing edge, the presence of a strong reverse flow immediately downstream of the jet may cause similar turning of the trailing-edge vorticity.

For the round hole, the realignment of leading- and trailing-edge boundary layer vorticity is extremely difficult to detect since the hole curvature makes these contributions indistinguishable from the sidewall vorticity. For a non-circular geometry such as a square or rectangle, the leading- and trailing-edge vorticity are plainly distinguishable from the sidewall vorticity. Thus, the selection of the square and rectangular holes enables us to separate the jet vorticies that comprise the kidney vortices.

By using these simpler geometries, the following questions can be addressed: (i) Can hole-exit geometry influence lift-off? (ii) Do the leading- and trailing-edge boundary layers simply cancel each other, or do they alter the effect of the sidewall boundary layer and contribute to the downstream kidney vortices?

These questions provide the framework for the present investigation. Question (i), the gross effect of hole geometry on lift-off, is presented first in §3 after a description of the experimental facilities and techniques (§2). The hole geometry is systematically changed so as to alter the lateral separation of the sidewall vorticies. This leads to a broad-brush picture: jet lift-off can be controlled by the width of holes, which determines the lateral separation between vortices.

Detailed study of these jets (§3) unfolds, unexpectedly, the double-decked structure of the nascent streamwise vortices: the first pair is located in the lower-deck and is what we call 'steady', and the second pair is located above in the intermittent upper deck. The first pair exhibits the same sense of rotation as the kidney-vortices and this is so regardless of the hole geometry.

On the other hand, the sense of rotation of the unsteady second pair in the upper deck depends on the hole geometry: for low-aspect-ratio holes, it is the same as the lower pair (i.e. an unsteady kidney pair) but for high aspect ratio, opposite to the lower pair (i.e. an unsteady 'anti-kidney' pair).

As discussed in §6, the contributions from the leading-edge boundary layers are linked, in fact, to this upper deck. We will find that the entrainment of crossflow momentum into the jet can warp the crossflow–jet interface, and cause streamwise realignment of the jet leading-edge vorticity. Depending on warping of the interface, the realigned streamwise vorticity is either the unsteady kidney or anti-kidney pair. While the unsteady kidney pair reinforces the kidney-vortices in the lower deck, the anti-kidney competes with the kidney vortices. The jet lift-off behaviour is then determined not only by the lateral separation between vortices but also by the interaction between the upper- and lower-deck vortices. It is precisely in this interactive effect that the details of the hole geometry enter and play a discriminating role. In §7, we will discuss that the similar warping of the trailing-edge vorticity, now caused by reverse flow, also induces an anti-kidney pair. These anti-kidney pairs again cancel the steady kidney pair of the lower deck.

In the light of this, the previously held view that the leading- and trailing-edge boundary layers simply annul each other appears to be in need of substantial

modification, at least in the present range of blowing ratio: they, instead, are actively engaged in the evolutionary process of the kidney vortices.

The results for the much studied round hole are presented in §8 and interpreted in the context of the other geometries.

All testing was done using water in both the jet and crossflow fluid. Since the density of both fluids is the same, the commonly used blowing ratio ($BR = \rho_j U_j / \rho_\infty U_\infty$, where ρ_j and U_j are the jet density and velocity, respectively, ρ_∞ and U_∞ are the crossflow density and velocity) is reduced to just the velocity ratio: $VR = U_j / U_\infty$. The range of VR used throughout the experiments is 0.4 to 2.0. The field of study is restricted to the vicinity of the hole, mostly to the flow immediately over the hole.

2. Experimental facility and techniques

The experimental techniques combined flow visualization with quantitative velocity measurements. Flow visualization using laser-induced fluorescence (LIF) was used to examine the basic vortical structures of the jet in the plane illuminated by a sheet of laser light. Particle image velocimetry (PIV) provided the two-dimensional velocity field, from which the corresponding vorticity component perpendicular to the laser sheet was calculated. Although the use of PIV enabled us to acquire important quantitative data, the resolution imposed by the camera pixel field limits its capability to capture fine-grained vortical structures as sharply as LIF does; thus, the two techniques complemented each other.

2.1. *Water tunnel and jet supply system*

The water tunnel is a closed-circuit recirculating facility with a 3.0 m $\times$ 0.7 m $\times$ 0.7 m glass test section. An acrylic flat plate, 1.0 m $\times$ 0.5 m, was suspended in the test section approximately 7 cm below the free surface of the tunnel. Two plate configurations were used, which differed only in the distance from the leading edge of the plate to the jet. For the flow visualization experiments, the jet was located 26 cm from the leading edge. Due to imaging considerations with the PIV system, the hole position was moved further downstream to a location 52 cm from the plate leading edge. The displacement thickness of the boundary layer corresponding to the former is 0.31 cm, the latter 0.44 cm. For further detail, see Haven (1996).

The jet fluid supply system is shown in figure 1. Velocity profiles taken at the exit plane of the jet with no crossflow showed that the settling chamber does not introduce bias into the crossflow jet measurements; see Haven (1996).

The jet fluid for the LIF experiments was prepared by mixing 2×10^{-4} grams of disodium fluorescein per litre of water. For the PIV experiments, the water in the preparation tank was seeded with 4 mm nylon spherical particles at approximately 7×10^{-4} grams per litre of water. The specific gravity of the nylon particles is 1.02.

2.2. *Laser-induced fluorescence technique*

LIF used a laser sheet generated by a nominal 5 W argon ion laser and a 1200 Hz scanning mirror to illuminate the jet fluid. As the laser sheet intersected the jet, the fluorescing jet fluid shows up as a white image when recorded on a CCD camera; the main flow, not seeded with fluorescein, appears dark. In the figures presented later, the images are flipped vertically so that the jet appears to be injected upwards rather than in the actual downwards direction.

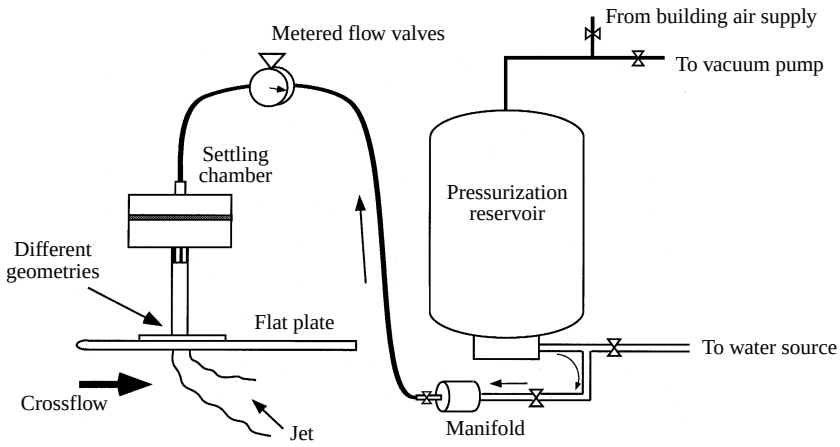

FIGURE 1. Jet fluid supply system.

Hole	Hole shape	Dimensions (cm) $D\times L$	Length (normal to page) (cm) H	Aspect ratio $AR=\frac{D}{L}$
1		1.34×3.66	25	0.37
2		1.75×3.50	25	0.5
3		2.48 dia	27	1.0
4		2.19×2.19	25	1.0
5		3.50×1.75	25	2.0
6		3.66×1.34	25	2.7
1a		1.95×5.27	14	0.37
6a		5.27×1.95	14	2.7

TABLE 1. Hole configurations

2.3. *Particle image velocimetry*

Quantitative flow field measurements were acquired using a TSI Incorporated PIV system, which measures the particle displacement within the laser sheet between two laser pulses. The particle locations, corresponding to each laser pulse, are recorded on a separate video frames using a modified, 640 pixel by 480 pixel, CCD camera. A cross-correlation algorithm is then run on each pair of images to determine the particle displacement in pixels. Once the particle displacements have been calculated, post-processing enables the calculation of velocity and vorticity. The time-averaged flow field was obtained by averaging three to five instantaneous snap shots. For more detail, see Haven (1996).

2.4. *Hole configurations*

The hole geometries used throughout the experiments are shown in table 1. The first six holes, with which the majority of LIF experiments and all of the PIV experiments were conducted, all have the same exit area. The remaining two holes, 1a and 6a, are scaled-up versions of holes 1 and 6, and were used to look closely at the fine-grained vortical structures. For all holes, the cross-section is constant along their pipe length.

Quantity	Dimensional designation	Multiplier	Non-dimensional designation
x-direction	x	$1/L$	x'
y-direction	y	$1/D$	y'
z-direction	z	$1/D_{hole3}$	z'
u-velocity	u	$1/U_\infty$	u'
v-velocity	v	$1/U_j$	v'
w-velocity	w	$1/U_j$	w'
Vorticity	ω	D_{hole3}/U_j	ω'

TABLE 2. Non-dimensional parameters

2.5. *Non-dimensionalization and colour-coding*

Non-dimensionalization of the quantitative measurements is accomplished as shown in table 2. The characteristic length used to non-dimensionalize the z-direction and vorticity was arbitrarily chosen as the diameter of the round hole, D_{hole3}. This was to allow for the recalculation of the vorticity, if necessary, directly from the value of ω' without the need to know the contributions from each of the non-dimensionalized derivatives. The dimensional vorticity components themselves are defined in the usual manner. The z-locations for the laser sheet were non-dimensionalized using the same reference length for all holes to facilitate comparison of data for the different holes.

The general colour coding for the PIV results is blue for negative values of vorticity and velocity, red for positive, and white for the values near zero. The PIV plots employ the 'pointillistic' method: the magnitude of the measured velocity or vorticity at a given point is represented by the associated colour at that point.

The hole passage length-to-diameter ratio, H/D_{hole3}, for holes 1–6 is approximately 10. For all experiments using holes 1–6, the crossflow was maintained at 8 cm s^{-1}; therefore, the velocity ratio is proportional to the jet velocity, $VR \propto U_j$. The jet velocity was determined by dividing the volume flow rate by the exit area of the hole. For holes 1a and 6a, the crossflow velocity was reduced to 5.4 cm s^{-1} in order to attain the same velocity ratios with the existing jet supply system.

The Reynolds number, based on jet cross-stream dimension, D, and crossflow velocity, U_∞, ranged from 1040 to 2900.

3. Effect of hole geometry on jet trajectory

In response to the first question raised in §1, we investigate here how changes in the exit geometry of holes alter the attachment of jets to the surface.

3.1. *Kidney vortices due to sidewall vorticity*

According to the view initially proposed by Scorer (1958), kidney vortices are the downstream manifestation of vorticity initially arising from within the sidewall boundary layer of the hole passage. As illustrated in figure 2 for a rectangular hole geometry, the sidewall of the hole generates vorticity aligned with the x-direction. This vorticity, after undergoing an intermediate growth stage, eventually appears in a far downstream plane oriented in the (y, z)-plane as the kidney-vortices, represented as $(\omega_x, -\omega_x)$. A more precise description, however, must also consider vorticity which is not initially aligned in the x-direction. All vorticity originating within the hole is subject to twisting and turning as the jet interacts with the crossflow. This means that vorticity generated on the front and back walls of the hole, though not initially aligned in

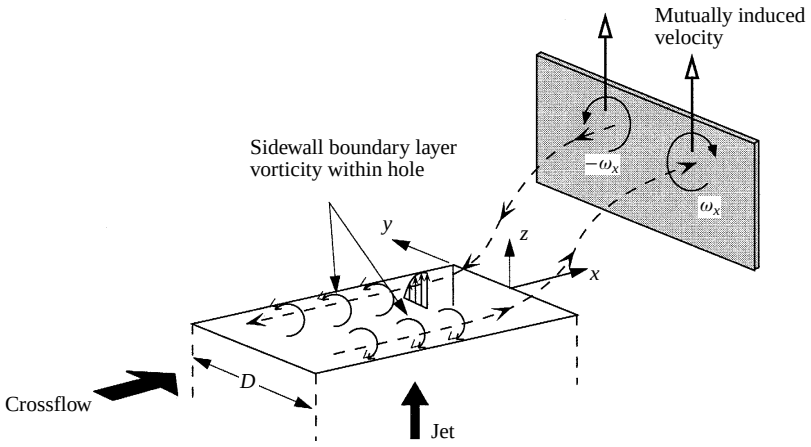

FIGURE 2. Kidney vortices due to hole sidewall vorticity.

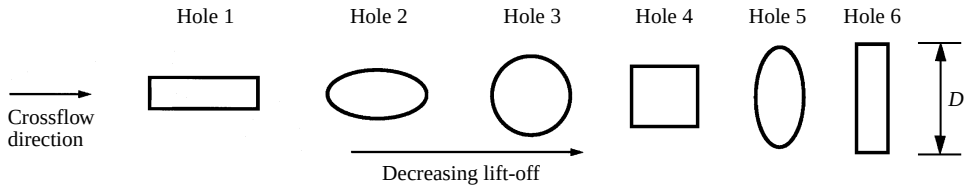

FIGURE 3. Trend of jet lift-off with hole geometry.

the x-direction, can be turned such that additional x-components of vorticity may appear in the (y, z)-plane. The crossflow boundary layer can likewise be realigned due to the interaction with the jet. We shall return to the subject of vorticity realignment later as it turns out to have an important bearing on the lift-off behaviour of the jet. For now, however, we will ignore this realigned vorticity and follow Scorer's view by focusing attention on the hole sidewall boundary layer.

3.2. *Link between kidney vortices and jet lift-off*

When one looks at only the vorticity generated by the sidewall of the hole, it is reasonable to expect that the lateral separation of the kidney vortices can be manipulated by changing the hole geometry: even for the same cross-sectional hole area, the larger the cross-stream dimension of the hole, D, such as in the case of hole 6 (high-aspect-ratio rectangle), the larger the lateral distance separating the kidney vortices. The increased separation decreases the mutual induction due to the vortex pair, each of which induces an upward velocity on the other. The net result is that the jet tends to stay near the surface. On the other hand, as the kidney-vortices are brought closer together by decreasing the cross-stream dimension, as in the case of hole 1 (low-aspect-ratio rectangle), the mutual induction increases and the jet lifts off the surface. By proceeding along this line of reasoning, one can arrive at the 'spectrum of shaped holes' displayed in figure 3 for holes 1 to 6. Note here that the cross-sectional area of all holes is the same.

Confirmation of these trends is shown in figures 4–6 for $VR = 1.6$. Figure 4 is the view perpendicular to the crossflow, which shows the kidney vortices at the downstream side of the hole, $x' = 1$ (the details of the caption such as the upper deck and lower deck and explanation for the arrows will be given in §4).

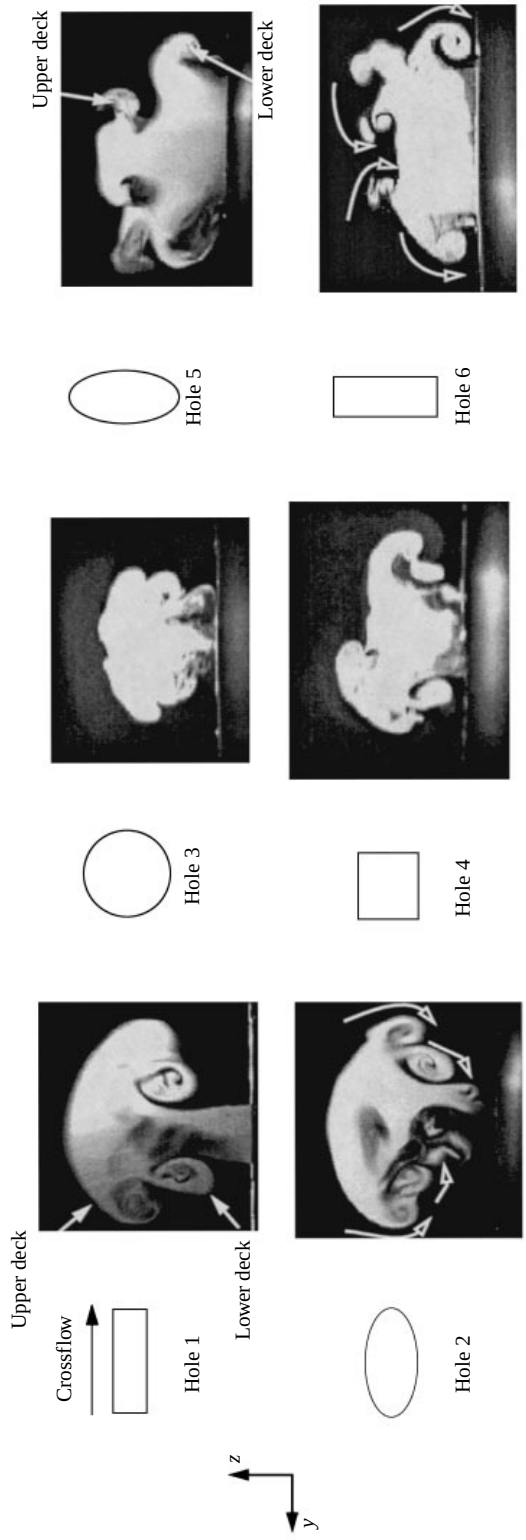

FIGURE 4. Laser-induced fluorescence (LIF) images showing kidney-vortices at downstream edge of hole, $x' = 1.0$, for $VR = 1.6$. Seeded jet is white and unseeded crossflow dark.

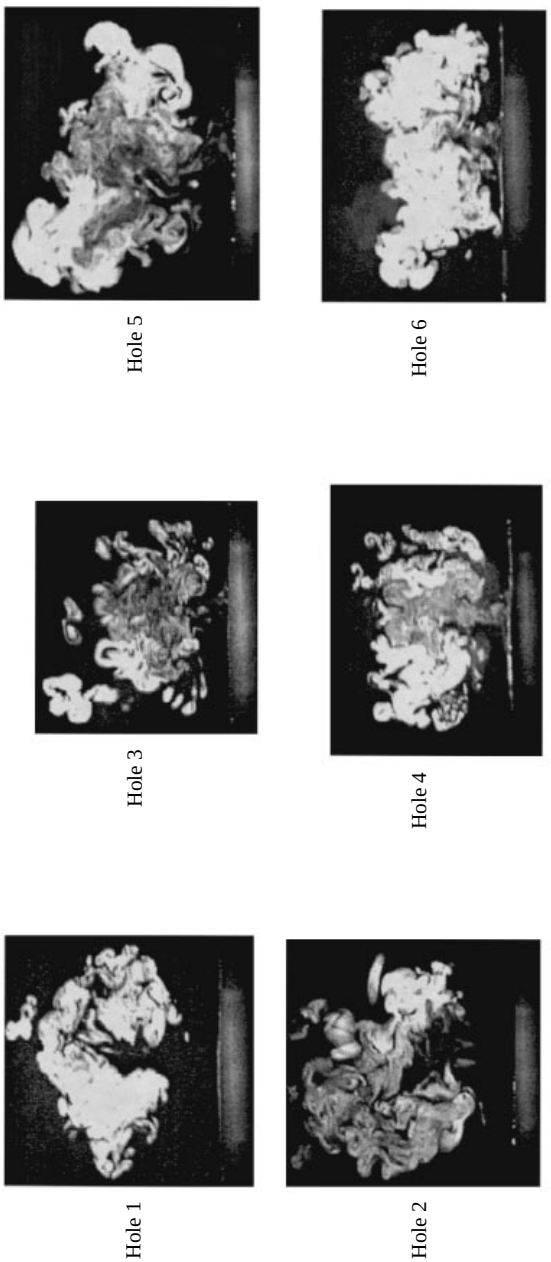

FIGURE 5. LIF images at 5.08 cm downstream of hole trailing edge, $VR = 1.6$.

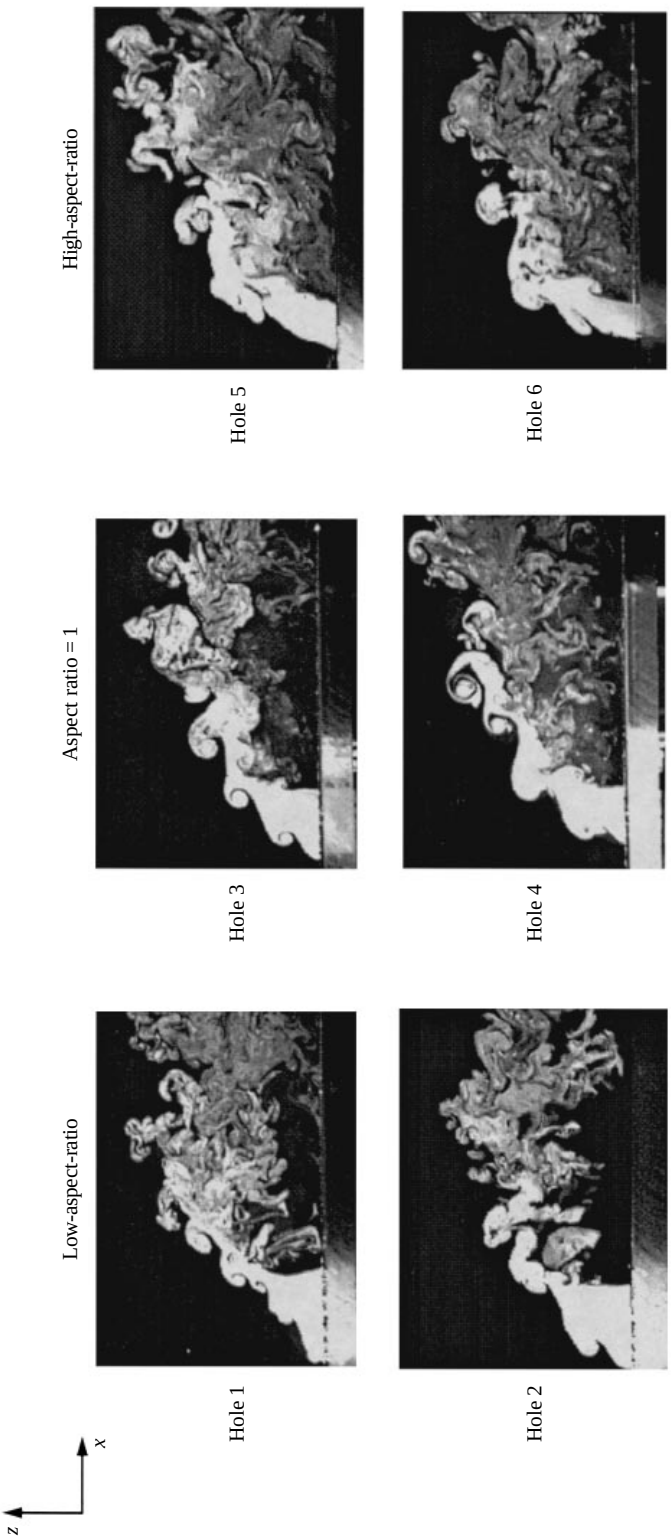

FIGURE 6. LIF images of jet trajectory along the centerline for $VR = 1.6$.

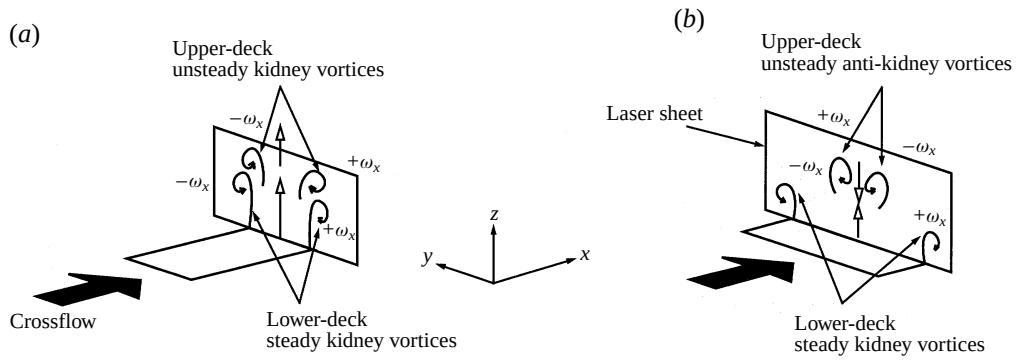

FIGURE 7. Double-decked structure showing (*a*) unsteady kidney pair in the upper deck for low-aspect-ratio rectangle and (*b*) unsteady 'anti-kidney' pair for high-aspect-ratio rectangle. Hollow arrows represent mutually induced velocities between either lower-deck or upper-deck vortex pairs.

As mentioned, the lift-off of the jet is expected to be affected by the lateral position of these kidney vortices with respect to each other. This can be seen in figure 5 as the laser sheet is moved 5.08 cm downstream of the hole trailing edge. Comparison of holes 1–6 shows a marked decrease in the jet lift-off as hole aspect ratio increases. The mutual induction between the streamwise vortices for hole 1 is responsible for the dark crossflow boundary layer fluid being drawn into the bottom of the jet.

The trajectory along the jet centreline in the (x, z)-plane, shown in figure 6, confirms the change in lift-off behaviour seen in the cross-sectional views of figures 4 and 5. From holes 1–6, there is a progressive increase in the degree of jet attachment to the wall. Although these are instantaneous images, they are typical in that they represent the overall trend. In contrast to 'shaped' holes, where jet attachment is influenced by both their non-circular geometry and increase in cross-sectional area toward the exit, here the change in lift-off behaviour is only due to the two-dimensional geometry of the hole.

By coincidence, Liscinsky, True & Holdeman (1995) also investigated holes of similar shapes. Contrary to our results at $VR = 1.6$, they did not find any noticeable difference in jet trajectory at $VR = 2.9$. Obviously, once the jet is blown off the surface at the higher blowing ratios, the hole geometry appears to have little effect on its subsequent behaviour.

4. Double-decked structure

Even a glance at the cross-sectional view at the trailing edge, figure 4, reveals that for each jet configuration the streamwise vortices consist of more than a single counter-rotating pair. They appear to be stacked on top of one another as double-deck structures and are labelled as 'lower' and 'upper' vortices.

The lower-deck vortices are termed 'steady' in that they are always present, although they are perturbed by the unsteadiness of the upper deck. The sense of rotation of the 'steady' lower deck is the same as the kidney vortices: viewed from upstream, $+\omega_x$ on the right, $-\omega_x$ on the left, shown schematically in figure 7.

The upper-deck vortices ride intermittently over the top of the steady ones. They may exhibit a rotational direction either in the same sense as, or opposite to, the steady lower-deck vortices. The unsteady vortices that rotate in the same sense as the lower-deck vortices are called the unsteady kidney pair; the unsteady vortices that

rotate opposite to the lower deck are referred to as the unsteady anti-kidney pair. Whether the upper deck is a kidney or anti-kidney pair depends on the hole geometry and can be classified in the following way:

class 1: unsteady kidney vortices for *low-aspect-ratio* rectangular and elliptical, and square and round holes; these vortices are shown schematically in figure 7(*a*) as $+\omega_x$ on the right, and $-\omega_x$ on the left for the low-aspect-ratio rectangle; and

class 2: unsteady anti-kidney vortices for *high-aspect-ratio* elliptical and rectangular holes, shown in figure 7(*b*), as $-\omega_x$ on the right and $+\omega_x$ on the left for the high-aspect-ratio rectangle.

With reference to figure 7(*a*), the unsteady kidney-vortices induce an upward velocity (top hollow arrow), which adds to that of the lower deck (bottom hollow arrow) and promotes the jet lift-off; while the induced velocity of the anti-kidney vortices, shown in figure 7(*b*), has a cancelling effect and prevents the jet lift-off.

The two instantaneous LIF pictures of figure 8(*a*) display the intermittent nature of the upper deck for a square hole belonging to class 1 at $VR = 1.6$: the picture on the left captures the unsteady kidney pair in the upper deck, while the one on the right shows only the steady kidney pair in the lower deck. (For the other holes, the upper deck is similarly intermittent at $VR = 1.6$, but the frames captured in figure 4 all correspond to the cases where the upper decks are visible.)

For the same square hole, figure 8(*b*) shows the double-decked structures now in the time-accurate vorticity maps obtained by PIV. With regard to the magnitude of vorticity, at $t = 198$ ms, for instance, the maximum values of the unsteady pair denoted by (b_+, b_-) are (+12.8, −13.0), while those of the steady pair (a_+, a_-) are (+17.1, −16.6). The time average of the instantaneous vorticity plots is also given in figure 8 (*b*, right). The maximum values of the time-averaged vorticity for the unsteady kidney pair denoted by ($\bar{b}_+$, $\bar{b}_-$) are (+7.6, −7.5); they are comparable with those of the steady pair ($\bar{a}_+$, $\bar{a}_-$), (+11.1, −12.4). Both tend to lift the jet off the plate.

The frequency of this unsteady pair recorded on the video film appears to be the same as the vortices shed from leading edge observable in the trajectory plane of figure 6 (approximately 5 Hz for $VR = 1.6$ and $U = 8$ cm s^{-1}) although the precise determination of the frequencies was difficult due to the fact that neither phase averaging nor external forcing was used.

Figure 9(*a*) shows additional time-averaged vorticity plots for four different x'-locations along the exit plane of the square hole: $x' = 0$, 0.46, 0.82, and 1.0. (The one for $x' = 0.82$ is the same as observed on right of figure 8.) The corresponding lateral velocity plots (figure 9(*b*)) show the side spillage of the jet along the front half of the hole. Further downstream, as the jet exits the hole near the trailing edge, the steady kidney vortices lift off the plate, resulting in a lateral induced velocity below the vortices and toward the centreline. The vertical velocity plots in figure 9(*c*) show the upward velocity of the jet surrounded by the negative vertical velocity, which is induced by the kidney pair on the sides. (The negative vertical velocity at the leading edge of the hole, $x' = 0$, will be discussed in §6.1.)

For the high-aspect-ratio rectangle, the anti-kidney vortices in the upper deck, previously observed at $VR = 1.6$ in figure 4, are again displayed in figure 10 (top) at $VR = 1.0$ and 2.0; the LIF picture at $VR = 1.0$ shows the anti-kidney pair most conspicuously. It also appears distinctly in the time-averaged PIV data in figure 10(*a*) for $VR = 2.0$ at $x' = 0.45$, 0.60, and 1.04. The magnitude of the anti-kidney pair is comparable with that of the steady kidney pair: for instance, at $x' = 0.6$, the maximum values of the anti-kidney pair denoted by ($\bar{b}_-$, $\bar{b}_+$) are (−6.4, +7.0), while those of the kidney pair ($\bar{a}_+$, $\bar{a}_-$) are (+10.9, −11.2). Plots of the lateral velocity, v',

in figure 10(*b*) show the same side spillage as for the square hole (figure 9*b*). Here, because the kidney vortices in the lower deck stay closer to the surface, the lateral flow toward the centreline happens only at the downstream edge of the hole ($x' = 1.04$).

The vertical velocity plots in figure 10(*c*) exhibit low-velocity regions near the centerline of the hole (compare with figure 9*c* for a square hole). These depressions correspond to the anti-kidney vortex pairs observed in figure 10(*a*): the anti-kidney pair is counteracting the effect of the steady kidney pair to lift off the jet.

Thus, the influence of hole geometry on the jet trajectory observed in §3 is not just due to the change in the lateral separation of vortices. Unexpectedly, the hole geometry is also found to be a discriminator in inducing, in the upper deck, either an unsteady anti-kidney pair or kidney pair; they either cancel or reinforce the effect of the lower kidney vortices. The origin of these lower- and upper-deck structures is discussed next.

5. Lower-deck structure

5.1. *Sidewall vorticity*

As the jet leaves the hole, the crossflow occupying the space above the jet acts like a ceiling. This forces the jet sidewall boundary layer to turn laterally outward by 90° and spill over the edges of the hole. The presence of the crossflow surrounding the outboard sides of the jet then acts like a wall, preventing its further lateral spread. The complete confinement by the 'ceiling', 'wall', and the test plate, or 'floor', boxes in the spilled boundary layer and forces it to roll up, and convection makes it into a concentrated spiral vortex sheet. The sidewall vorticity, while spiralling downstream, is also tilted upwards by the streamwise increase of the vertical velocity, which results from the 'blockage' imposed on the frontal part of the jet by the crossflow. The steady kidney vortices of the lower deck are the result of this spilling, spiralling and upward tilting of the sidewall boundary layer vorticity, shown in figure 11(*a*) (this figure is a more precise version of the rough sketch of figure 2). The vector plot in figure 11(*b*), obtained by PIV for the square hole at $VR = 0.8$, shows the laterally outward motion of the jet fluid as it leaves the hole (at this VR and x-position, the upper deck is undetectable).

The lower-deck kidney vortices or spiral vortex sheets resemble the upside-down wing-tip vortices, a concept exploited most explicitly by Broadwell & Breidenthal (1984) in modelling the far-field jet trajectory. It is known that trailing vortices from a wing tip are stable (Moore 1976; Saffman & Baker 1979) and this may be a reason for the steadiness of the lower-deck kidney vortices. The coexistence of steady lower-deck and unsteady upper-deck vortices may not be unusual when we consider that in wings steady trailing vortices and unsteady wake vortices can coexist.

The aforementioned skewness of the w'-profile due to the blockage imposed by the crossflow becomes most pronounced at lower blowing ratios, as exemplified in figure 12(*a*) (left) for the low-aspect-ratio rectangle, hole 1, at $VR = 0.8$. (The negative vertical velocity, w', at the leading edge of the hole corresponds to the downward velocities induced by both the horseshoe vortex and the jet leading-edge vortex at the hole exit, to be discussed in §6.1.) The corresponding ω_z' distribution at $z' = 0.12$ is shown in figure 12(*a*) (right). Even at the higher blowing ratio of $VR = 1.6$, shown in figure 12(*b*) together with the other shapes, the vorticity induced in the z-direction clearly follows the contours of each hole and becomes greater near the trailing edge. This increase in ω_z toward the trailing edge can

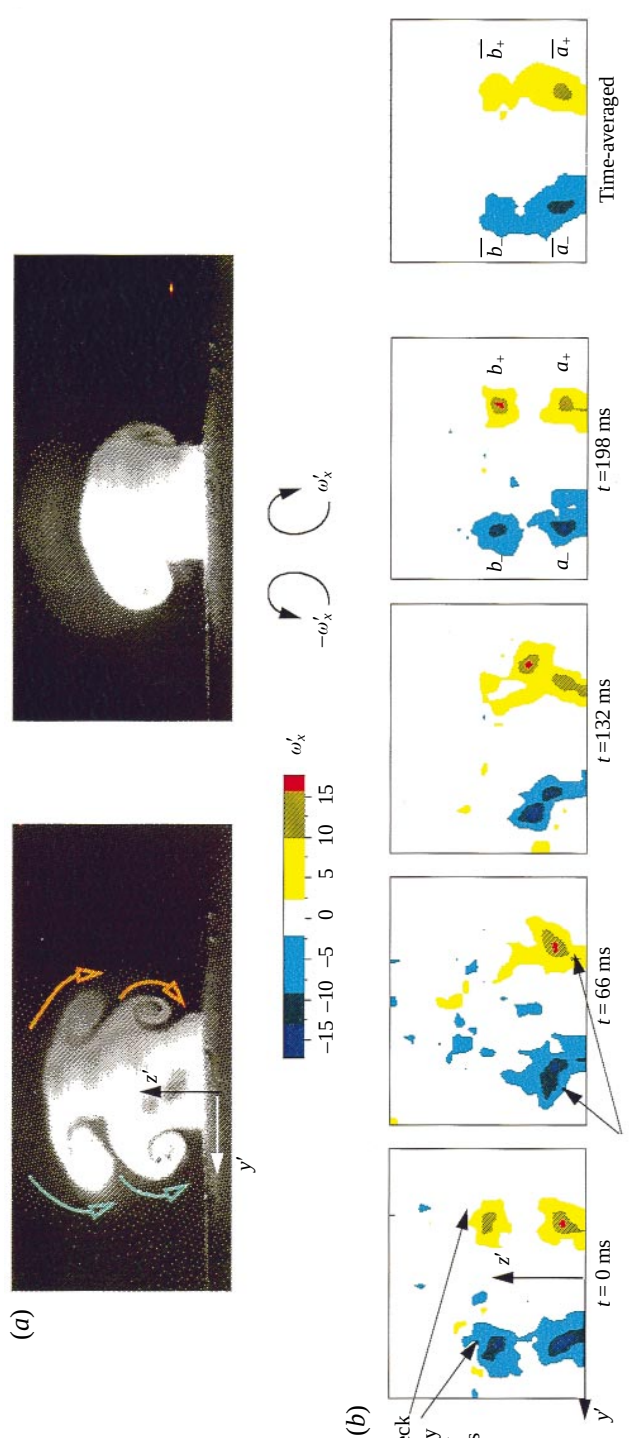

FIGURE 8. (*a*) LIF pictures at $VR = 1.6$ and $x' = 1.0$. (*b*) Time-accurate and time-averaged PIV plots of vorticity at $x' = 0.82$, showing the double-decked structure of an unsteady kidney-vortex pair riding on top of the 'steady' kidney-vortex pair. Square hole (hole 4) at $VR = 1.6$. The view is from upstream. The PIV plots employ the 'pointillistic' method: the magnitude of the measured velocity or vorticity at a given point is represented by the associated colour at that point.

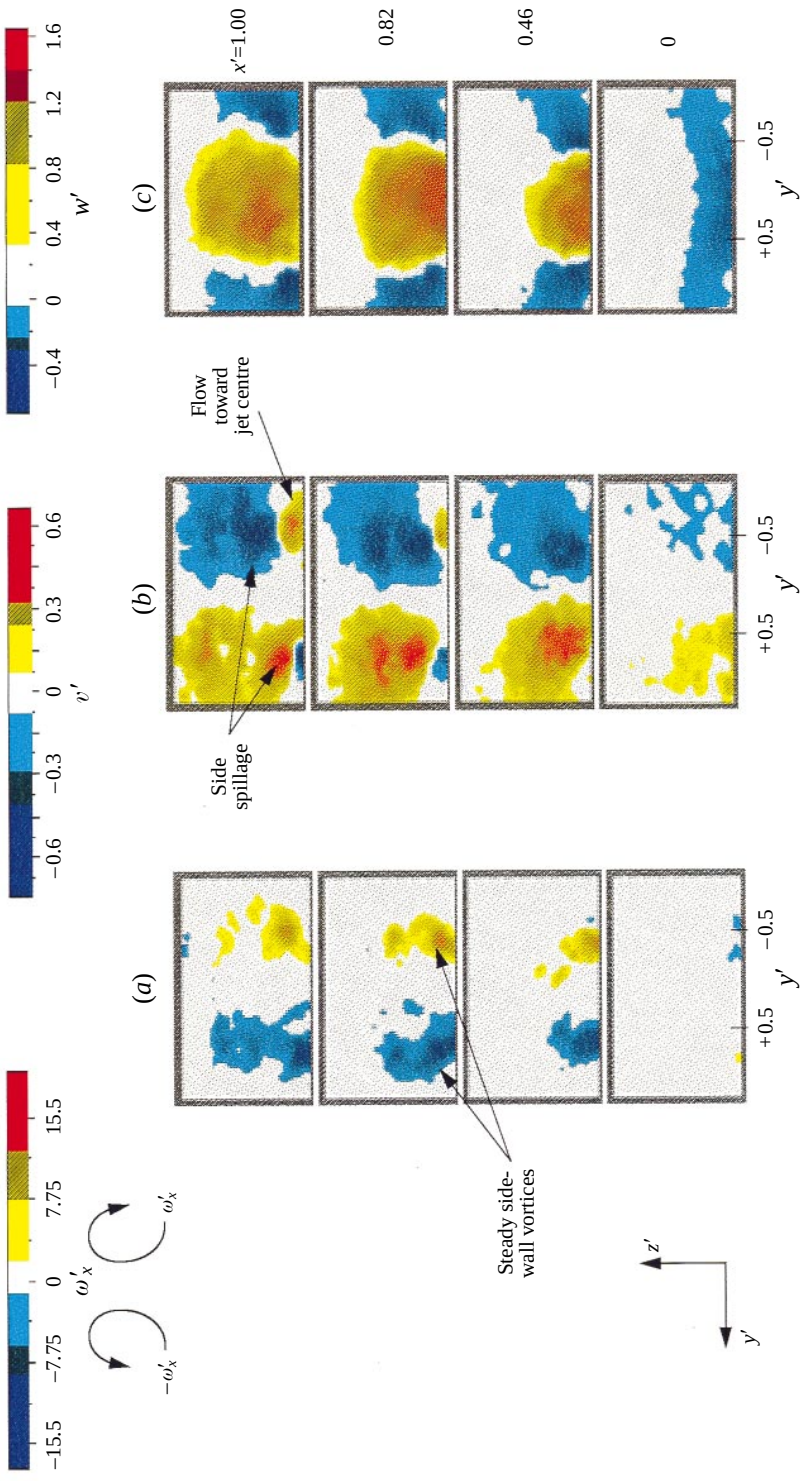

FIGURE 9. Square hole (hole 4). Time-averaged PIV colour plots: (*a*) vorticity, (*b*) v'-velocity, (*c*) w'-velocity for $VR = 1.6$. The view is from upstream.

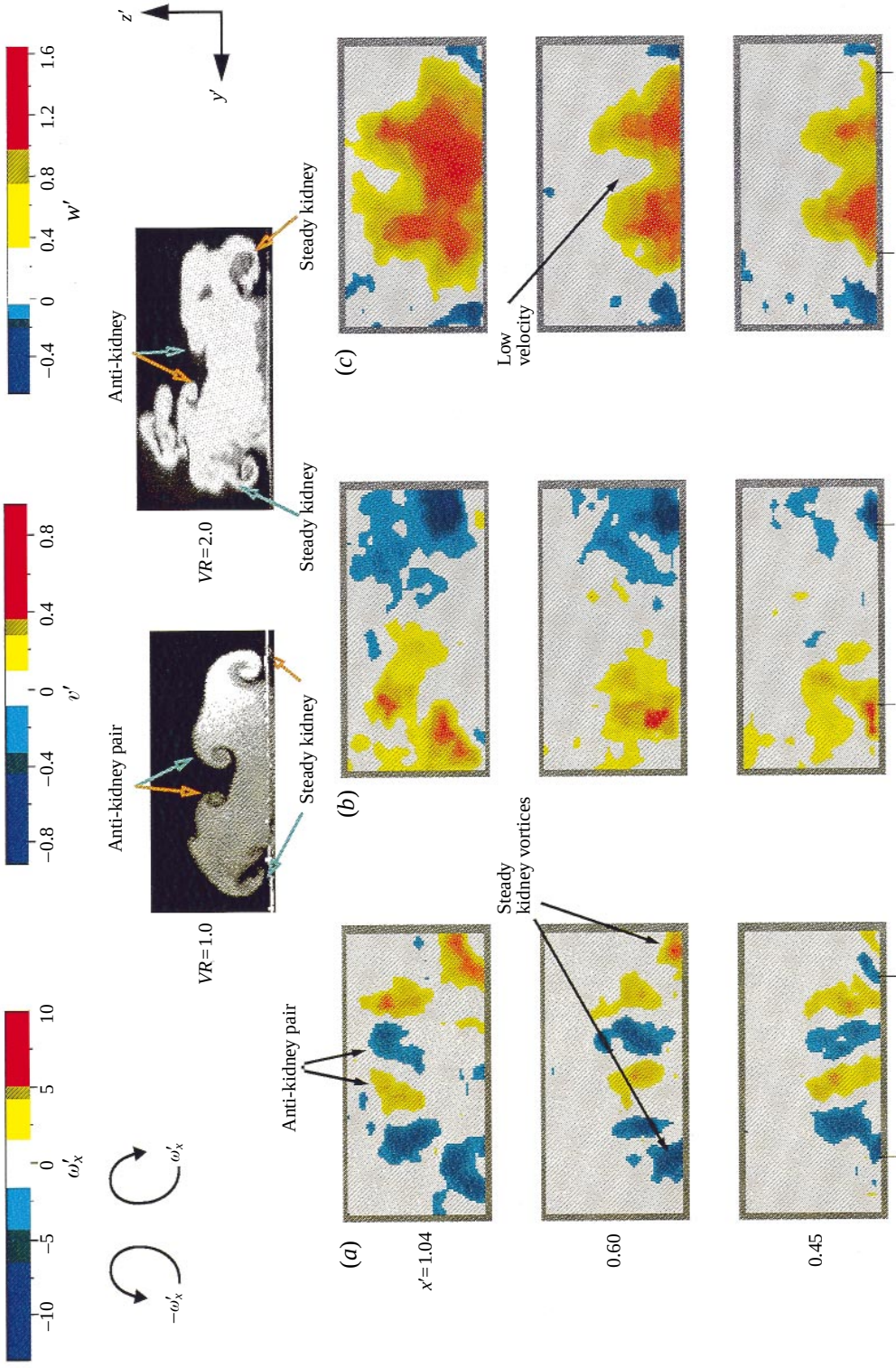

FIGURE 10. LIF (top) and time-averaged PIV colour plots (bottom) for high-aspect-ratio rectangle (hole 6). LIF pictures at the trailing edge; left at $VR = 1.0$, right at $VR = 2.0$. All PIV plots are at $VR = 2.0$; (*a*) vorticity, (*b*) v'-velocity, (*c*) w'-velocity. The view is from upstream.

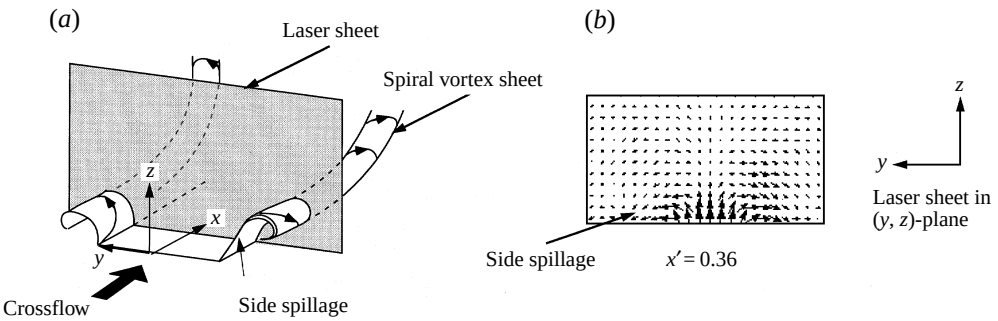

FIGURE 11. (*a*) Steady kidney vortices due to sidewall spillage. (*b*) Time-averaged PIV vector plot for square hole (hole 4) at $x' = 0.36$ and $VR = 0.8$.

be attributed to the increased jet velocity near the trailing edge (cf. the broken line of figure 12*a* left), which increases the tilting of the jet sidewall vorticity and aligns more of the jet vorticity in the z-direction. (In viewing the vortical structures shown here and elsewhere, it is important to keep in mind that these images correspond only to the vorticity component projected on each plane of the laser sheet.)

5.2. *Leading-edge vorticity; corners*

We will divide discussion of the leading-edge vorticity into two parts: (i) the vorticity near the corners of the hole leading edge to be considered here in relation to the lower-deck vortices, and (ii) the vorticity at the centre of the jet to be discussed in §6 in connection with the upper-deck vortices. At the leading-edge corners of the hole, near the sidewalls, the leading-edge vorticity spills out sideways and combines with the aforementioned steady spiral sheet of the sidewall boundary layer. This behaviour is seen in two different cross-sectional views of the jet for the high-aspect-ratio rectangle (hole 1a) in figure 13: views parallel to the plate and perpendicular to the crossflow. In both views, only the leading edge of the jet was seeded with two traces of fluorescein dye injected inside the hole at $z = -2.1$ cm from the exit.

In the parallel view (a–a section), the dye is observed to spill outward as it exits the hole from the leading edge. Although the leading-edge vorticity is initially aligned parallel to the a–a plane, it still appears here as out-of-plane vorticity, ω_z, due to its subsequent upward tilting.

Perpendicular to the crossflow (b–b section), the cross-section of the jet shows that the dye has been drawn to the centre of the steady sidewall vortices. This indicates that a portion of the leading-edge jet boundary near the corner is being turned in the direction of the crossflow; it then intertwines and amalgamates with the spiral vortex sheet of the sidewall boundary layer. Thus the leading-edge vorticity near the corners, as well as the sidewall vorticity, are the nascent form of kidney vortices far downstream. (The upward titling of the spiral sheet may be observed in three pictures taken at different x-positions by following the upward movement of the dye traces within the vortex cores.)

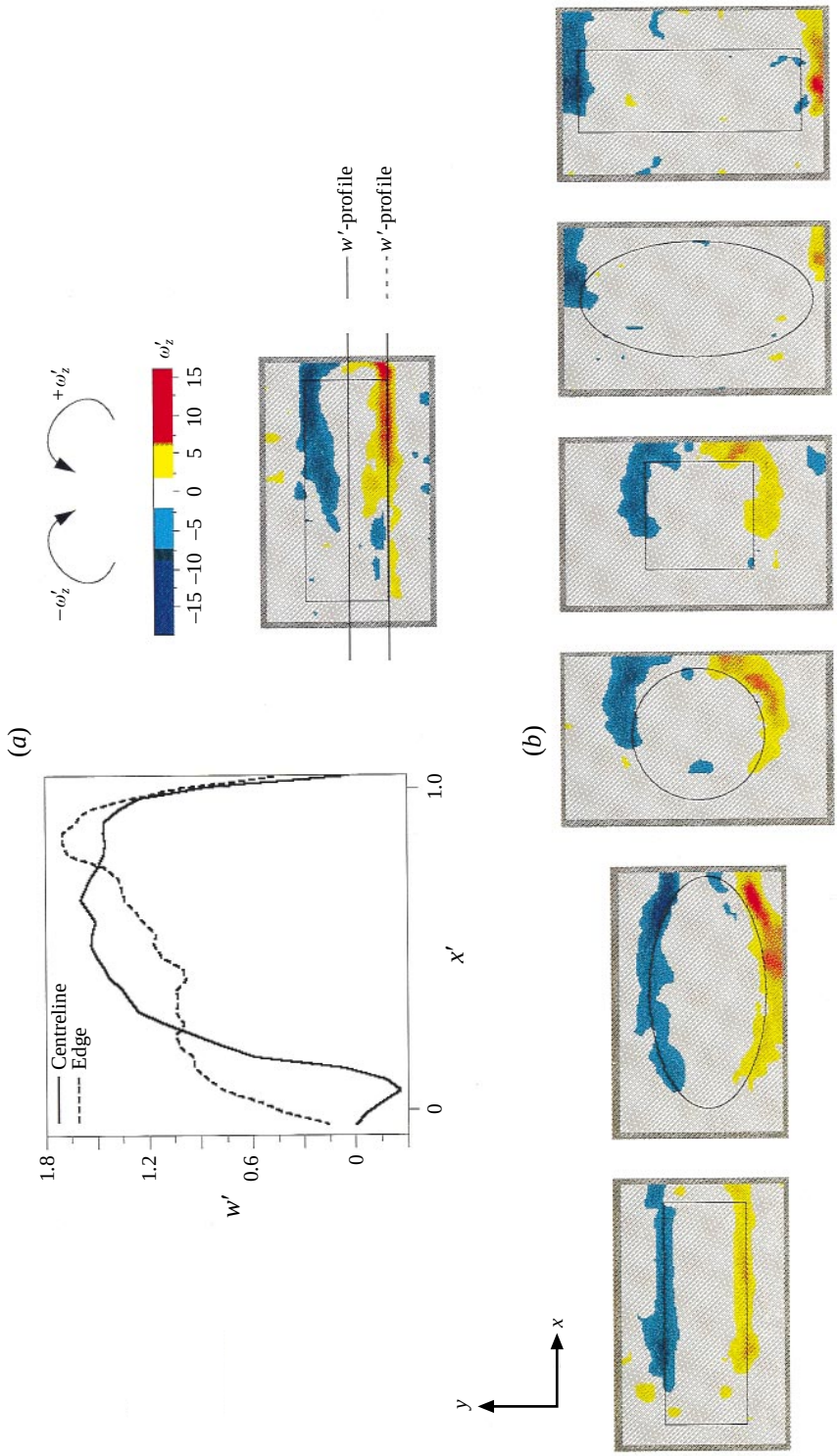

FIGURE 12. Time-averaged w' plot and ω_z' distributions at $z' = 0.12$; (*a*) $VR = 0.8$, (*b*) $VR = 1.6$. The holes are viewed from above.

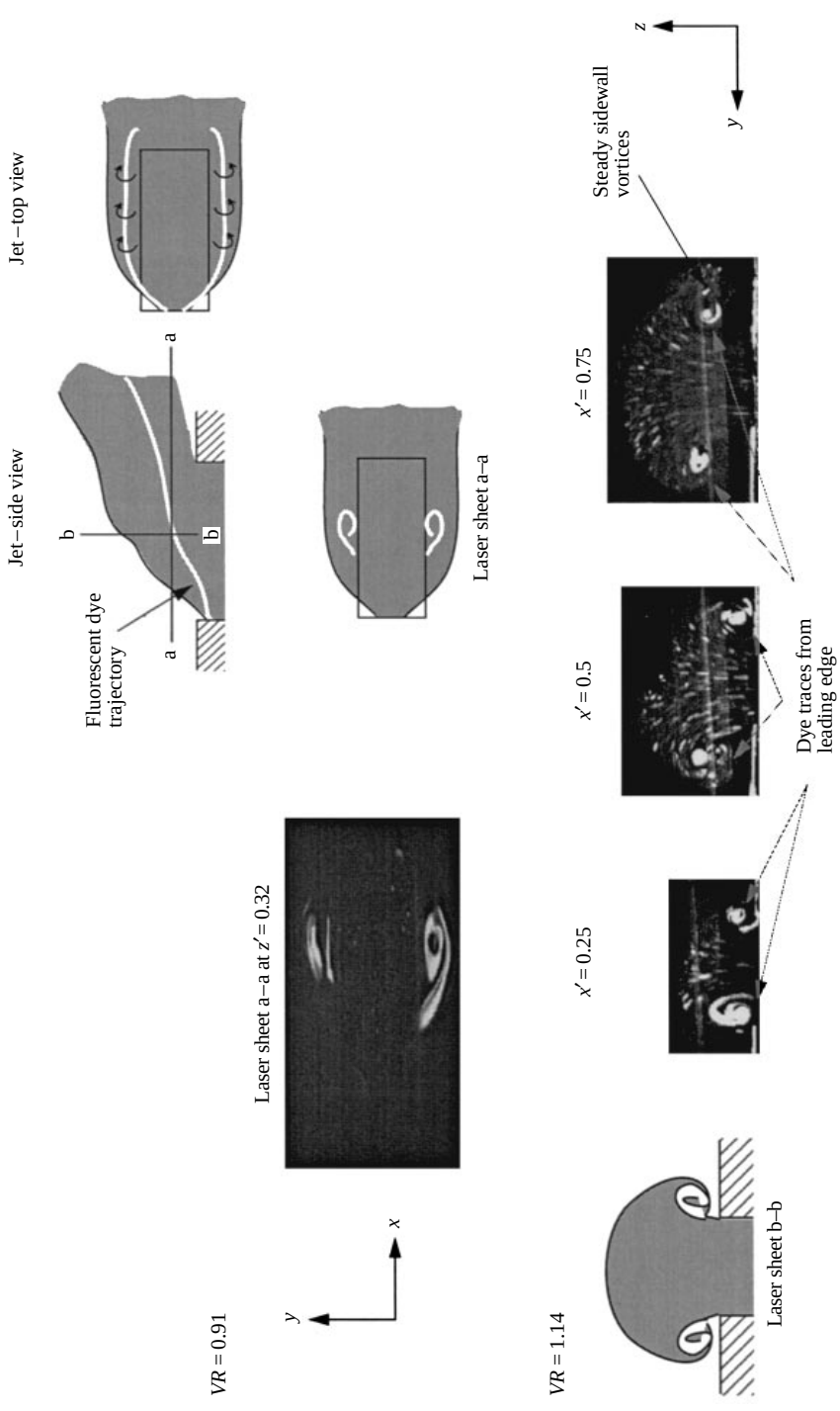

FIGURE 13. Leading-edge boundary layer near the corner combines with sidewall boundary layers. High-aspect-ratio rectangular hole (hole 1a).

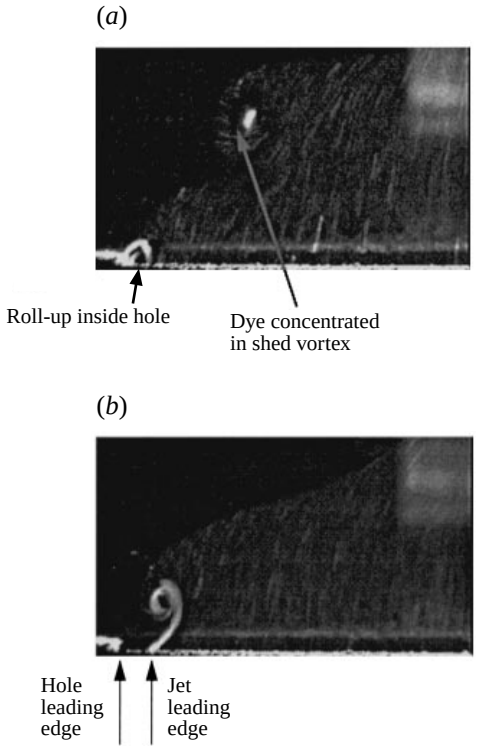

FIGURE 14. (*a*) Roll-up and (*b*) shedding of leading-edge vorticity for low-aspect-ratio rectangle (hole 1a). $VR = 1.6$.

6. Upper-deck structure

6.1. *Leading-edge vorticity; central region–initial development*

The central portion of the leading-edge vorticity is affected by the horseshoe vortex formed just upstream of the jet. Although the horseshoe vortex does not appear to penetrate the jet at the leading edge, its presence can be felt well within the jet passage. The influence of the horseshoe vortex can be seen in w'-velocity plots of figure 9(*c*) for the square hole at $x' = 0$. The induced velocity of the horseshoe acts to suppress the jet flow inside the hole leading edge. This, coupled with the induced downward velocity due to the roll-up of the leading-edge vorticity discussed below, results in a negative vertical velocity, w', at the leading edge of the hole (blue areas of figure 9*c*, $x' = 0$).

To the jet leading edge, the crossflow appears as a partial cover (Andreopoulos & Rodi 1984); the adverse pressure gradient thus imposed on the jet leading-edge boundary layer by this blockage causes it to roll up, separate from the passage wall and shed periodically. This jet separation and roll-up, observed earlier by Andreopoulos (1982) and more recently by Kelso *et al.* (1996) for a round hole, mirrors the crossflow separation as a horseshoe vortex. Figure 14(*a*) shows the roll-up of jet vorticity inside the low-aspect-ratio rectangular hole. In this same picture, the previously shed vortex shows a trace of fluorescent dye at its centre. At another instant, figure 14(*b*), the leading-edge shed vortex is seen just outside of the hole.

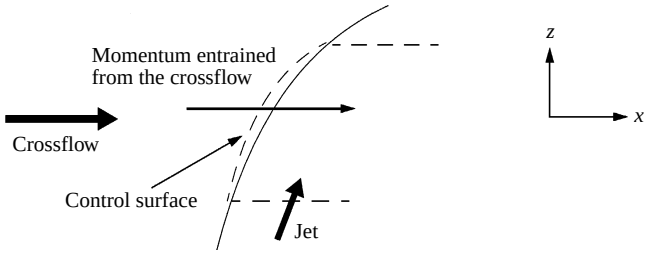

FIGURE 15. Control surface at the jet-crossflow interface.

6.2. *Realignment of leading-edge vorticity*

As the boundary layer emerges from the hole leading edge, dynamical interaction with the crossflow realigns its vorticity; this is an important issue sidestepped so far, which we now discuss. When we construct a control surface at the interface of the frontal part of the jet and the crossflow (figure 15), the momentum entrained from the crossflow into the jet acts as the surface force imposed on the jet (*e.g.* Hoult & Weil 1972). The amount of momentum entrained at a point depends on the local 'resistance' of the jet. The stronger the local resistance, the less momentum is entrained locally. Since the local resistance is not expected to be the same from the jet center to the corners, the entrained crossflow momentum or surface force would change accordingly (more on this in §6.4). As a result, the interface is warped in the direction normal to the paper, or y-direction.

A simple heuristic model problem for the warping of the leading-edge vortex sheet is presented here to illustrate how the vorticity within the deformed interface can realign itself to induce either an unsteady anti-kidney pair or kidney pair of the upper deck.

The dynamic equation that governs the distribution of vorticity ($\boldsymbol{\omega}$) in the velocity field ($\boldsymbol{u}$) of present interest is the incompressible vorticity transport equation given by

$$\frac{\mathrm{D}\boldsymbol{\omega}}{\mathrm{D}t} = (\boldsymbol{\omega}\cdot\nabla)\boldsymbol{u} + \nu\nabla^2\boldsymbol{\omega}. \tag{1}$$

It is important to note that there are no vorticity source terms in equation (1). This means that all vorticity within the flow comes from the imposed initial and/or solid wall boundary conditions. The use of the vorticity equation, where pressure does not appear explicitly, is most convenient for the subsequent interpretation of the PIV results, because PIV measures velocity and vorticity rather than pressure.

In examining the vorticity realigned by the warping of the jet vortex sheet, we can neglect the viscous diffusion since the effect of diffusion would be very small in the near field, compared to the vorticity realigned by the stretching and turning of the vortex sheet due to the crossflow momentum. The governing equation then becomes

$$\frac{\mathrm{D}\boldsymbol{\omega}}{\mathrm{D}t} = (\boldsymbol{\omega}\cdot\nabla)\boldsymbol{u}. \tag{2}$$

To render the leading-edge warping problem tractable, we pose and solve a corresponding transient model problem. In this model problem, the discrete vortices of the rolled-up shear layer are smeared into a vortex sheet in order to examine the broad effect caused by its gross deformation.

The vortex sheet, which initially corresponds to the one at the leading edge of a free jet, is suddenly subjected to the crossflow. The jet then begins to be deflected and its interface warped by the influx of the crossflow momentum. Before the crossflow

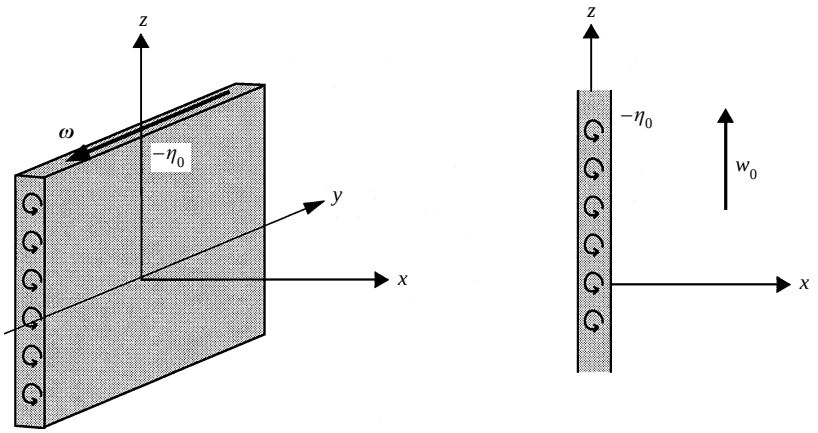

FIGURE 16. Definition sketch for the first model problem.

is turned on, an infinite vortex sheet lies in the (y, z)-plane (figure 16). On one side of the vortex sheet, at $x > 0$, the jet exits the hole vertically with a velocity $w = w_0$. The induced velocity due to the vortex sheet is ignored: for $x < 0$, $w = 0$. There are no other velocity components. The vorticity is concentrated in the vortex sheet and its y-component is given by $\omega_y = -\eta_0$, where $\eta_0 > 0$; its x- and z-components are initially zero.

At $t = 0+$, the crossflow is turned on. We assume complete entrainment of the crossflow into the jet at the interface. Both the horizontal and vertical velocities are independent of x and z, and vary only with y. The transverse velocity remains zero:

$$u = u(y), \quad w = w(y), \quad v = 0.$$

Under the above assumptions, the three vorticity transport component equations are reduced to the following:

$$x\text{-component:}\ \frac{\partial \omega_x}{\partial t} + u(y)\frac{\partial \omega_x}{\partial x} = -\eta_0 \frac{\mathrm{d}u}{\mathrm{d}y}, \tag{3a}$$

$$y\text{-component:}\ \frac{\partial \omega_y}{\partial t} = 0, \tag{3b}$$

$$z\text{-component:}\ \frac{\partial \omega_z}{\partial t} + u(y)\frac{\partial \omega_z}{\partial x} = -\eta_0 \frac{\mathrm{d}w}{\mathrm{d}y}. \tag{3c}$$

According to the present formulation, new vorticity arising from the variation of u and w in the y-direction and present outside the vortex sheet is simply convected downstream, without interacting with the vorticity contained within the vortex sheet. Thus, the vorticity outside the vortex sheet can be decoupled from the vorticity within and dropped from the left-hand side of equations (3a)–(3c). Therefore, the above quantities ω_x, ω_y and ω_z refer only to the vorticity *embedded* in the vortex sheet; they are delta functions, being zero outside the vortex sheet.

The only physically relevant solutions of equations (3a)–(3c) are

$$\omega_x = -\eta_0 t \frac{\mathrm{d}u}{\mathrm{d}y}, \quad \omega_y = -\eta_0, \quad \omega_z = -\eta_0 t \frac{\mathrm{d}w}{\mathrm{d}y}. \tag{4a–c}$$

Equation (4a) shows that a streamwise component of vorticity, ω_x, is induced on the vortex sheet by the lateral variation in the streamwise velocity, u. For example,

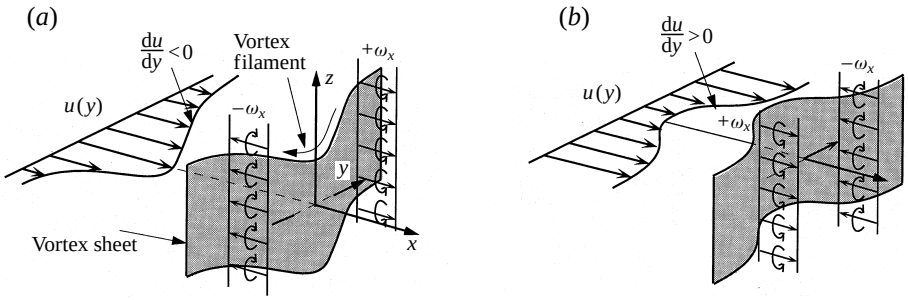

FIGURE 17. Warping of vortex sheet. (*a*) 'Concave' warping and 'anti-kidney' pair, (*b*) 'convex' warping and kidney pair.

consider the $u(y)$ distribution shown in figure 17(*a*), which corresponds to weak jet resistance at the centre. The warping yields positive ω_x for $y > 0$, where $\mathrm{d}u/\mathrm{d}y < 0$, and negative ω_x for $y < 0$, where $\mathrm{d}u/\mathrm{d}y > 0$; this will be referred to hereafter as concave (with respect to the jet) warping of the frontal surface and it corresponds to the anti-kidney pair. On the other hand, if $u(y)$ is such as shown in figure 17(*b*), which corresponds to strong jet resistance at the centre, the warping referred to as convex yields a kidney pair.

In applying the above transient results for the steady problem, time, t, may be replaced with the vertical distance from the hole, z. (In the steady problem, u and w on the left-hand side of the x-component of (2) are functions of x, y and z. Besides, compared to the unsteady problem, there are two extra terms on its right-hand side: $\omega_x\,\partial u/\partial x$ and $\omega_z\,\partial u/\partial z$. However, as long as one is interested in the warping near the hole exit and at the interface, $x = 0$ and $z = 0$, we can approximate u and w by their leading terms, which are dependent on y only. Furthermore, near the leading edge where one can take $\omega_z = 0$ and assume $|\partial u/\partial x| \ll |\partial u/\partial y|$, equation (4*a*), with t replaced with z/w, becomes a steady solution.)

Like the streamwise vorticity, equation (4*c*) shows that a vertical component of vorticity, ω_z, is induced by a variation in the vertical velocity, w. This result will be used in discussing the tilting of the trailing-edge vorticity (§7.2).

6.3. *Unsteady kidney pair from the leading edge*

As pointed out (§4), the frequency of the upper-deck vortices corresponds to the shedding frequency of the leading-edge vortices observed in the trajectory plane, the (x, z)-plane along centreline (figure 6). In fact, the unsteady upper deck is none other than the cross-plane manifestation of the leading-edge vortices caused by the just-mentioned warping of the frontal interface. As just discussed, the way in which the jet–crossflow interface at the leading edge is warped determines the sign of the vorticity as it passes through the laser sheet.

Figure 18(*a*) shows the frontal halves of the horizontal cut or (x, y)-plane view for low-aspect-ratio rectangle and ellipse, and a round and a square hole; in spite of the intermittent nature of the flow field, the prevailing characteristic of the frontal interface of these jets is convex, relative to the jet. Figure 18(*b*) shows convex bending of a single representative vortex filament contained in the convexly warped frontal interface which is initially aligned along the y-axis within the hole. Once shed from the hole, the leading-edge vortices embedded in the warped interface become bent in the streamwise direction and appear, in the (y, z)-plane, as discrete periodic vortices in the upper deck: the unsteady vortex pair with the same sign as the kidney-vortex

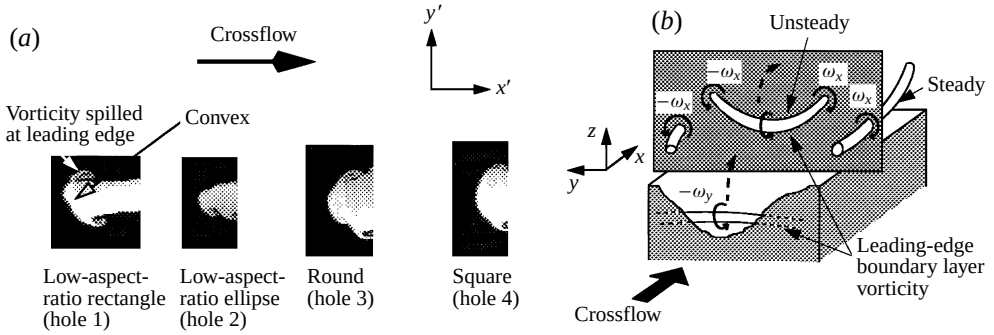

FIGURE 18. Convex warping (*a*); $VR = 2.0$, $z' = 0.26$. Induced unsteady kidney vortices (*b*).

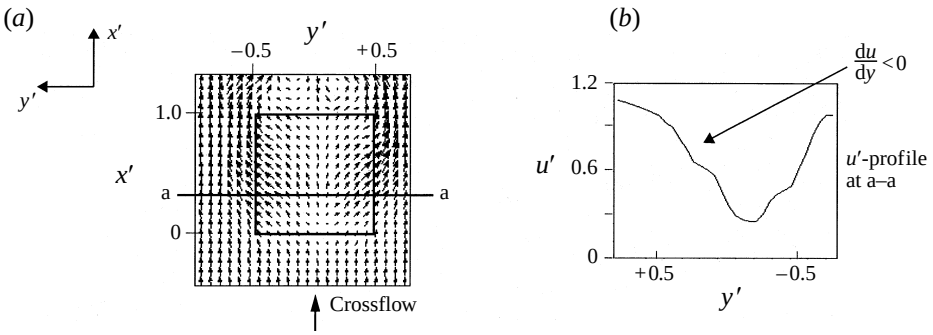

FIGURE 19. (*a*) Time-averaged vector plot and (*b*) u'-velocity for square hole (hole 4) at $z' = 0.32$, $VR = 1.6$.

pair. For all these holes – low-aspect-ratio rectangle and ellipse, and square – the upper decks are indeed unsteady kidney vortices (figures 4 and 8; see also Haven (1996) for additional data for the low-aspect-ratio ellipse, which include the PIV results substantiating further the presence of unsteady kidney pair).

The presence of convex warping of the jet front surface for a square hole, for instance, may also be substantiated from the streamwise velocity profiles, u', in the plane parallel to the plate at $z' = 0.32$, shown in figure 19. According to equation (4*a*), where t is now replaced by z, the lateral variation in u, $\mathrm{d}u/\mathrm{d}y$, indicates that the leading-edge vortex sheet is being warped to induce convex bending and an unsteady kidney pair: negative ω_x for $y > 0$, $\mathrm{d}u/\mathrm{d}y > 0$ and positive ω_x for $y < 0, \mathrm{d}u/\mathrm{d}y < 0$ (note that in figure 19(*b*) $y > 0$ on the left, $y < 0$ on the right).

(A recent flow visualization result for a square hole, presented by Ajersch *et al.*. (1995), shows the movement of an unsteady vortex pair over five consecutive flow visualization video images. However, their interpretation of these vortex structures differs from the one given above.)

6.4. *Unsteady anti-kidney pair from the leading edge*

As already mentioned (§4), for the high-aspect-ratio rectangle and ellipse the unsteady vortices from the leading edges form an anti-kidney vortex pair. For the high-aspect-ratio rectangle, hole 6, the presence of an anti-kidney pair has already been shown in figures 4 and 10, where the entire jet is dyed.

In a subsequent experiment using the larger area rectangular hole, hole 6a, *only* the jet leading-edge boundary layer was seeded with fluorescein by injecting dye inside

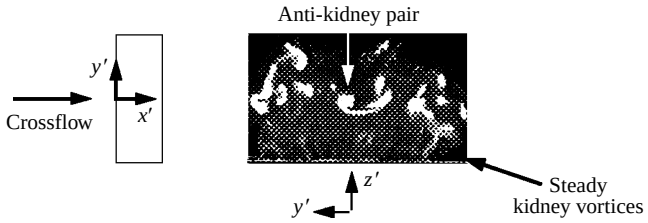

FIGURE 20. Anti-kidney pair for high-aspect-ratio rectangle, (hole 6a). Jet leading edge dye-traces at midpoint, $x' = 0.5$, $VR = 1.6$.

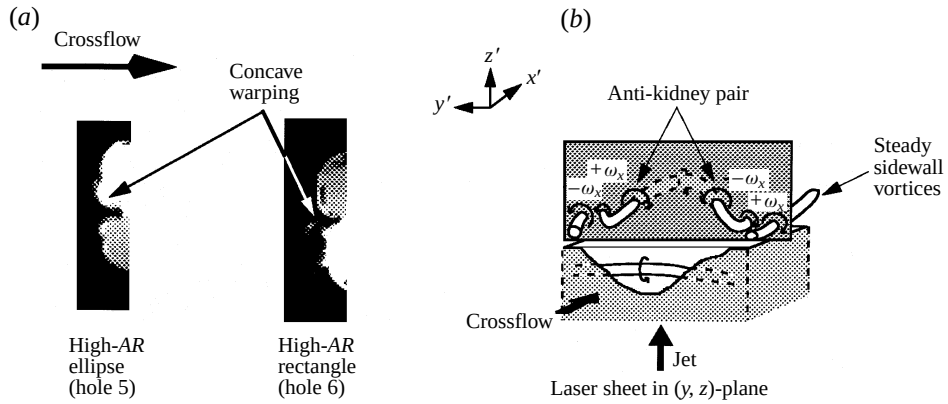

FIGURE 21. Concave warping (a); $VR = 2.0$, $z' = 0.26$. Induced unsteady anti-kidney pair (b).

the hole passage. The picture in figure 20, taken at the midpoint of the hole, shows the dye from the leading edge pooling in the area where an anti-kidney vortex pair is present. This explicit evidence verifies that the leading-edge vorticity manifests itself as an anti-kidney pair riding over the top of the jet.

For the high-aspect-ratio rectangle and ellipse, the paramount characteristic of the frontal interface is concave, as observed in figure 21(a). In contrast to convex warping of figure 18, this concave warping induces a streamwise vorticity component, ω_x, having the sense of rotation of the anti-kidney pair, as illustrated in figure 21(b) for a representative vortex filament (the convex bending near the corners corresponds to sideways spillage of the leading-edge vorticity of §5.2).

As a cross-check of the anti-kidney pair, figure 22 shows the velocity vector plot and u'-velocity profile for $VR = 1.6$ in the horizontal plane at $z' = 0.52$. In the u'-velocity profile, a peak is present near the centre, while for the square hole, a valley was present there (cf. figure 19).

Near the centre, the sign of the lateral variation of u, du/dy, is therefore reversed from that for the square hole and gives rise to an anti-kidney pair: positive ω_x for $y > 0$, $\mathrm{d}u/\mathrm{d}y < 0$, and negative ω_x for $y < 0$, $\mathrm{d}u/\mathrm{d}y > 0$.

Whether the frontal interface warps to give a convex or concave form is connected and consistent with the jet lift-off behaviour. For low-aspect-ratio holes, whose jets tend to lift off the surface easily, the jets appear to the crossflow like a solid cylinder, having an open wake region with room for the crossflow to fill in; this diverts the crossflow from the upstream to the wake region and results in the acceleration of the crossflow around frontal corners (see in figure 19, the increased u'-velocity near the corners, $y' = \pm 0.5$). By continuity, this reduces u' at the centre and provides 'relief'

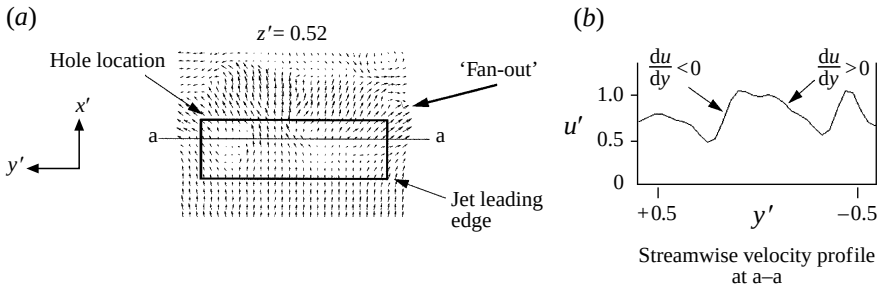

FIGURE 22. Time-accurate u'-distribution for high-aspect-ratio rectangle (hole 6) at $z' = 0.52$, $VR = 1.6$.

to the frontal surface. Thus the frontal interface assumes the convex shape. However, jets from high-aspect-ratio holes, which stay adhered to the surface (in the present range of VR), appear to the crossflow as a 'ground cover', assuming a fanned out shape (see figure 22*a*). There is no 'relief' provided by the wake so the central portion of the frontal interface bears the full brunt of entraining momentum or surface force, resulting in caved-in concave warping. (If this were the case, one would expect that at higher VR, when even the jet from the high-aspect-ratio holes starts to lift off, the concavity of the frontal interface should disappear. Recent tests at $VR = 4.5$ in fact confirmed that this indeed happens.) Since the jet lift-off itself is suppressed by the anti-kidney vortices induced by the concave warping, this intimate interdependence between the front and back of the jets highlights the three-dimensional dynamical interaction in crossflow jets.

See Haven (1996) for additional data taken for the high-aspect-ratio ellipse, which include the PIV results substantiating further the presence of an 'anti-kidney' pair.

7. Trailing-edge vorticity

Having discussed the leading-edge and sidewall boundary layers, here we present the role played by the trailing-edge boundary layer vorticity.

7.1. *Anti-kidney pair at the trailing edge*

The PIV data for both the low-aspect-ratio rectangle and ellipse reveal the presence of an anti-kidney pair at the trailing edge of the hole (Haven 1996). For the low-aspect-ratio rectangle, figure 23 shows the time-averaged vorticity aligned in the x-direction, ω_x, and the vertical velocity, w', at x'-locations of 0.57, 0.82, 0.90, 0.98, and 1.06. Near the trailing edge, the area between the vortex pairs is more chaotic than the previous holes. Despite this, a discernible anti-kidney vortex pair is present along the centreline, close to the surface of the plate. When one follows an anti-kidney pair, starting from the trailing edge and toward upstream, it appears to be lifted up. Near the middle of the hole ($x' = 0.57$), the anti-kidney pair is absent and only the lower-deck kidney pair appears. For this low-aspect-ratio rectangular hole, the unsteady kidney vortices in the upper deck are also prominent, as previously noted, and this is perhaps one reason for the chaotic appearance of the vorticity plots. Near the trailing edge, where the anti-kidney vortex pair appears, the vertical velocity profile of figure 23(*b*) shows low-velocity regions near the surface and centreline of the jet. The formation of this anti-kidney pair at the trailing edge is considered to arise from the warping of the trailing-edge boundary layer by the reverse flow downstream of the jet. The reverse

flow is to the trailing edge what the crossflow is to the leading edge; this will be discussed next.

7.2. *Reverse flow*

Shown schematically in figure 24(*a*) is the tilting up of the trailing-edge vorticity about its centre due to the upstream penetration of the reverse flow. This causes the vorticity, which is initially aligned in the y-direction, ω_y, to become realigned by the variation of the vertical velocity in the transverse direction, $w(y)$. As an example, figure 25(*a*) gives the w'-velocity profile at the downstream edge of the square hole, hole 4, which shows the expected peak near the centre of the jet. With reference to equation (4*c*), where, for the trailing edge, $-\eta_0$ is replaced by η_0, the sign change of the velocity gradient, $\mathrm{d}w/\mathrm{d}y$, on each side of the centreline suggests that a vortex pair aligned in the z-direction will be induced at the trailing edge of the hole by vorticity tilting. Flow visualization at a laser sheet position of $z' = 0.26$ (figure 25*b*) confirms that such a vortex pair $(\omega_x, -\omega_x)$ exists at the downstream corners of the hole. Such 'corner' vortices, which are also expected from the difference in the flow directions between the crossflow and reverse flow to be described shortly, are present for all other holes. Laser sheets at different z-locations show that these 'corner' vortices, appearing on the underside of the jet, remain well defined far off the plate surface (Haven, 1996).

The upward tilting of the trailing-edge vortex near its centre results in the induction of the negative u'-velocity or a reverse flow between the vortex pair (figure 24*a*). In addition, the lowered pressure in the wake (P_2 in figure 26(*a*) is less than P_∞, the far-field crossflow pressure), which is present to balance the centrifugal force acting on the curved jet, also causes a reverse flow in the wake. The PIV vector plot, figure 26(*b*), shows the presence of such a reverse flow in the wake region of the square hole.

The streamwise velocity distributions processed from these vector plots on the (x, y)-plane, shown figure 27, display the presence of the reverse flow in the wakes of all holes, together with the reverse flow upstream of the holes caused by the horseshoe vortices. Particularly prominent among them is the deep upstream penetration of the reverse flow for the low-aspect-ratio rectangle and at $z' = 0.32$; the backflow is much more localized and penetrates far upstream of the trailing edge. The effect of this penetration may also be observed in the jet trajectory view of figure 6, where the lee side of the jet for the low-aspect-ratio rectangle (hole 1) is bent upstream; this is in contrast to the high aspect ratio rectangle and ellipse (holes 5 and 6), where the reverse flow does not penetrate upstream of the hole trailing edge.

The penetrating reverse flow at the trailing edge acts like a crossflow at the leading edge; the ensuing concave warping of the trailing-edge vortex sheet (figure 24*b*) thus induces an anti-kidney pair for the low-aspect-ratio rectangle and ellipse. The presence of the anti-kidney pair underneath the jet and at the surface of the plate suggests that the vortex filament at the trailing edge is most likely realigned while it is still within the hole. The anti-kidney pair is convected briefly by the reverse flow at the same time as it is lifted off the plate. Thus the anti-kidney pair is detectable only in the downstream half of the hole, as seen in figure 23(*a*); in the upstream half, only the kidney pair is present. The anti-kidney pair for the low-aspect-ratio rectangle also tends to mitigate the kidney pair of the lower deck, but, in contrast to the high-aspect-ratio rectangle, its appearance at the trailing edge is too late to counterbalance the action of the kidney pair in lifting-off the jet. (Even for the square hole, at the highest blowing ratio of 2.0, an anti-kidney pair is present at the trailing edge, along the centreline and close to the surface of the plate, see Haven (1996);

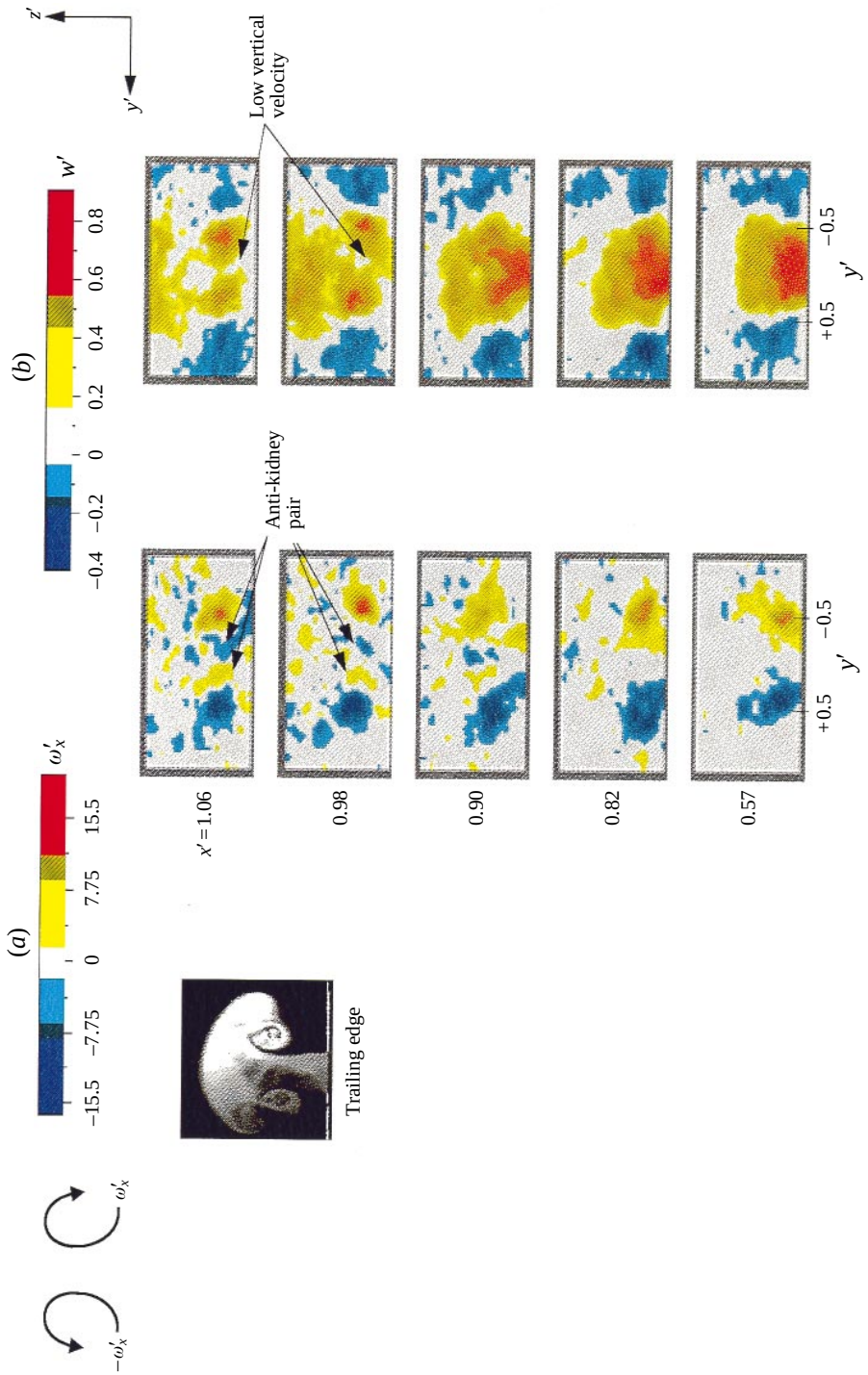

FIGURE 23. Time-averaged PIV colour plots for low-aspect-ratio rectangle (hole 1) at $VR = 1.6$; (*a*) vorticity, (*b*) w'velocity. The view is from upstream.

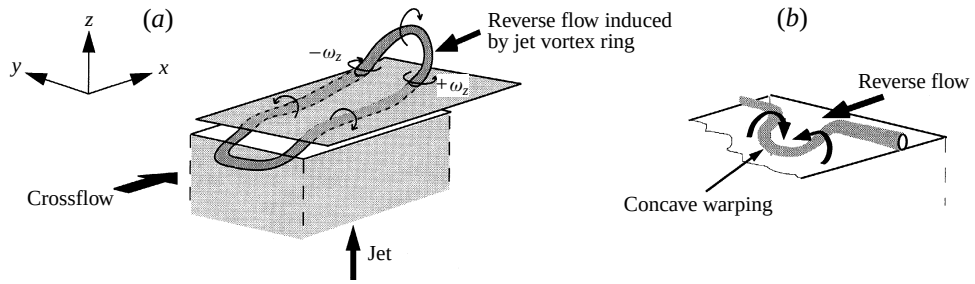

FIGURE 24. Trailing edge vorticity: (*a*) tilting (*b*) concave warping.

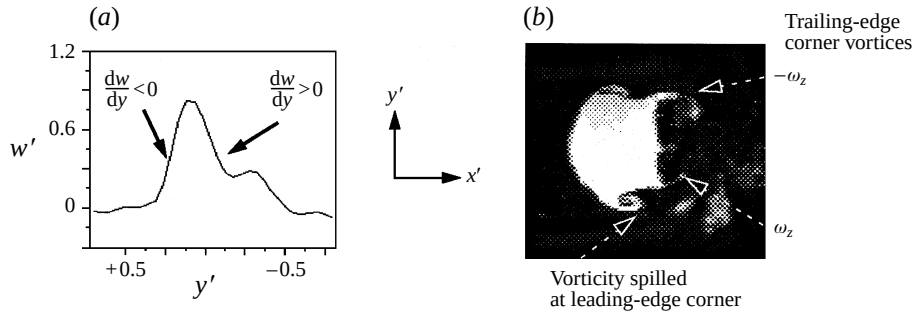

FIGURE 25. w'-profile and trailing-edge corner vortices of a square hole. $VR = 2.0$. (*a*) Time-averaged w'-velocity profile at trailing edge $x' = 1.0$; (*b*) LIF picture taken at $z' = 0.26$.

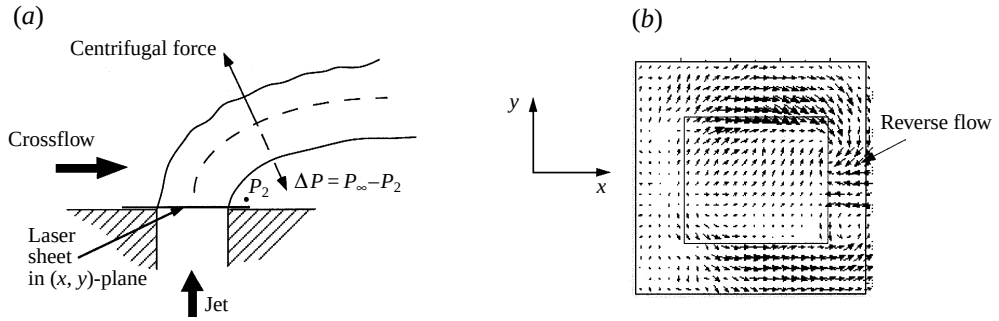

FIGURE 26. Reverse flow in wake: (*a*) lowered pressure in wake, (*b*) time-averaged PIV vector plot for square hole (hole 4), $z' = 0$, $VR = 1.6$.

this is again connected with the deep upstream penetration of the reverse flow at this blowing ratio.)

The reverse flow, in addition to causing the warping of the hole trailing-edge vorticity, draws the crossflow boundary layer fluid passing along the side of the hole into the underside of the jet. By this, the vorticity associated with the crossflow boundary layer diverted away from the jet by the horseshoe vortices is now pumped into the jet, where it combines with the tilted trailing-edge boundary layer and strengthens the downstream kidney vortices (Haven 1996).

Further downstream of the jet, large vortical structures resembling Kármán vortices have been observed, which become most conspicuous at $VR = 4$. These wake vortices, studied most recently by Wu, Vakili & Yu (1988), Fric & Roshko (1994),

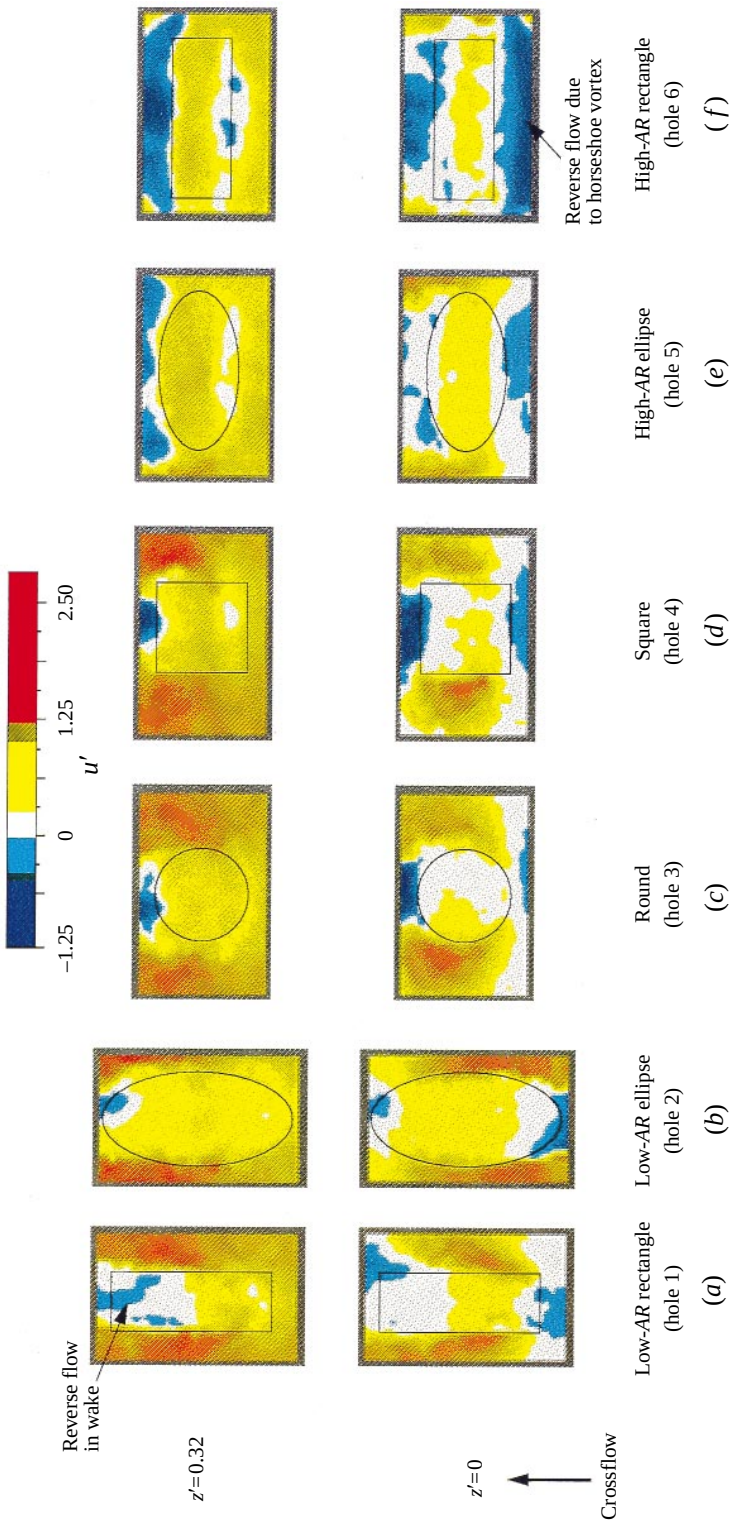

FIGURE 27. Time-averaged PIV plots for u' distribution showing the reverse flow in the wakes of all holes for $z' = 0$ and 0.32, plus the reverse flow upstream caused by the horseshoe vortices for $z' = 0$. $VR = 1.6$.

and Kelso *et al.* (1996), are shown to be composed only of crossflow boundary layer fluid. These vortices are then the only mechanism for introducing new vorticity into the jet once it leaves the hole. This new vorticity comes from the crossflow boundary layer, enters the bottom of the jet and may be transported upwards through the cores of the wake vortices by the so-called 'tornado effect' (Kurosaka *et al.* 1988; Hagen & Kurosaka 1993). Thus the far downstream kidney vortices consist of the aforementioned near-field vortices and the effect of wake vortices.

8. Round hole

The round hole is by far the most studied geometry for a jet in a crossflow. From the standpoint of understanding the vortex dynamics, however, the round hole is perhaps the most difficult because its curvature blurs the distinction between the vorticity arising from the leading edge, the sidewall, and the trailing edge. This is why we have delayed discussion of the round hole. With the preceding results for the other holes now to hand, we are ready to focus our attention to the round hole and face the question left unanswered in the past studies on round holes: besides the sidewall vorticity, which emerges from the two side points located furthest apart across the hole, how does the vorticity corresponding to the remainder of the hole circumference contribute to the kidney pair? In the present range of the blowing ratio, the answer is now obvious: vortices from the entire circumference contribute to the kidney vortices.

8.1. *Kidney vortices and anti-kidney pair*

Although the double-decked structures consisting of a steady kidney pair and an unsteady kidney pair may be long familiar to the reader, we will display them again for a round hole. This is not only for completeness, but also because for this much-studied round hole no clear distinction between the steady and unsteady pairs appears to have been drawn in the past investigations using such point measurements as three-dimensional hot-wire or laser Doppler velocimetry (LDV) techniques. On the other hand, PIV and LIF techniques, which can dissect and capture the complete flow field simultaneously, enable us to distinguish between the steady and unsteady vortex pairs even for a round hole.

The PIV plots of figure 28, taken at $x' = 0.73$, display the steady kidney pair located near the plate and the unsteady kidney pair riding on top of the jet, showing the intermittent characteristics of the unsteady kidney pair and steadiness of the lower-deck kidney vortices.

As discussed in §5.1, the steady kidney pair is caused by the lateral spillage and roll-up of the jet boundary layer; the unsteady kidney pair is caused by the combination of the intermittent roll-up of the leading-edge vortices and convex warping of the jet frontal surface (§6.3). The convex warping of the jet frontal surface for a round hole may be observed from figure 18 and its presence may be confirmed from the u'-velocity plot, figure 29(*b*), obtained at the a-a sections indicated in the vector plot of figure 29(*a*). The sign of the velocity derivative, $\mathrm{d}u/\mathrm{d}y$, is such that the vorticity generated has the same sense of rotation as the kidney vortices (cf. figures 18 and 19). Therefore, the intermittent passing of the leading-edge vorticity can be seen as unsteady kidney vortices riding on top of the steady structures.

The time-averaged PIV results for the x-component of vorticity and vertical velocity on the (y, z)-cross-sections located at various x positions for a $VR = 1.6$ are shown in figure 30. Compared to the instantaneous pictures of figure 28, the steady and unsteady kidney pair are smeared in the time average, except at $x' = 1.05$. Figure 30(*a*) also

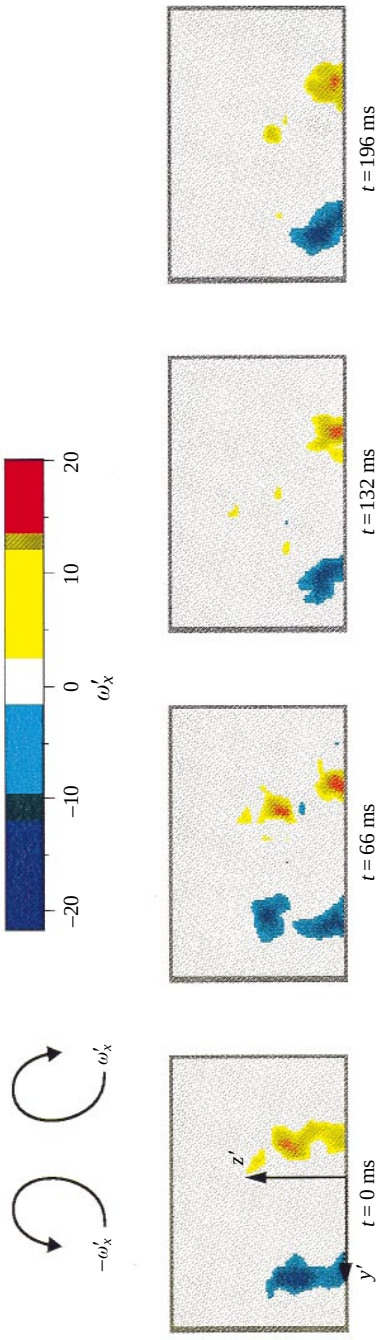

FIGURE 28. Time-accurate PIV vorticity plots for a round hole (hole 3) at $VR = 1.6$, $x' = 0.73$, showing an unsteady kidney vortex pair riding on top of steady kidney vortices. The view is from upstream.

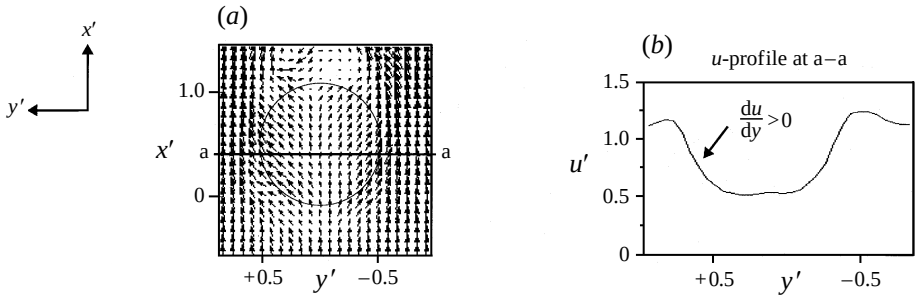

FIGURE 29. Streamwise velocity u' for round hole (hole 3) at $VR = 1.6$: (*a*) time-averaged vector plot at $z' = 0.32$, (*b*) corresponding u'-velocity profile at $z' = 0.32$ and $x' = 0.4$.

shows an anti-kidney vortex pair appearing near the surface of the plate at $x' = 0.97$; the maximum values of the anti-kidney pair denoted by $(\bar{b}_-, \bar{b}_+)$ are $(-3.0, +3.6)$ while those of the steady kidney pair at $(\bar{a}_+, \bar{a}_-)$ are $(+8.8, -7.3)$.

As discussed in §7, the anti-kidney pair is induced by the concave warping of the trailing-edge vortex sheet, which is caused by the reverse flow. The *u'*-velocity distribution of figure 27(*c*) shows the presence of the reverse flow focused at the trailing edge. (The anti-kidney pair is also present for $VR = 2.0$, but not at $VR = 0.8$ Haven (1996). The lack of an anti-kidney pair for the lower blowing ratio appears to be due to weaker reverse flow.) As noted in §7.1, the vertical position of the anti-kidney pair in figure 30(*a*) is again at the surface of the plate and underneath the jet, which tends to suppress the jet's vertical velocity at the centreline and near downstream edge of the hole. This is shown in the vector plot of figure 30(*c*), which displays the region of low-vertical-velocity fluid near the plate and at the centreline corresponding to the anti-kidney pair, together with the distinct steady kidney vortices at the sides of the jet. The anti-kidney pair for a round hole was previously reported by Moussa, Trischka & Eskinazi (1977), where a three-dimensional hot-wire was used to map the crossflow jet issuing from a round pipe at $VR = 3.48$. Their figure 17, which displays contours of ω_x in the (y, z)-plane, shows a small anti-kidney pair above the kidney pair at positions corresponding to the present $x' = 0.5$ (their figure 17*a*), $x' = 0.75$ (figure 17*b*), and $x' = 1.5$ (figure 17*d*). However, at the trailing edge of the hole, $x' = 1.0$ (figure 17*c*), there is no anti-kidney pair, contrary to our data. Instead of the present mechanism based on the warping of the trailing edge boundary layer, the explanation offered by Moussa *et al.* (p. 76) is '... each bound vortex [i.e. the kidney vortices in the present terminology] must generate in the cross-stream an equal and opposite rotation with equal circulation'. This explanation appears to be at odds with the fact that no new vorticity can be generated within the flow. Curiously enough, with the exception of Moussa *et al.*, no other subsequent studies† on the round hole, or any other shaped hole, all of which used point-measurements, has reported the anti-kidney pair.

8.2. *Additional comments*

The other characteristics of the round jet are similar to those found in the literature. For instance, the u'-velocity profiles shown in figure 31, measured by PIV at two points

† After the initial submittal of the present paper, Professor Kelso kindly informed us of a forthcoming paper (Kelso, Lim & Perry 1997), which reports an observation about an additional vortex pair for a round jet.

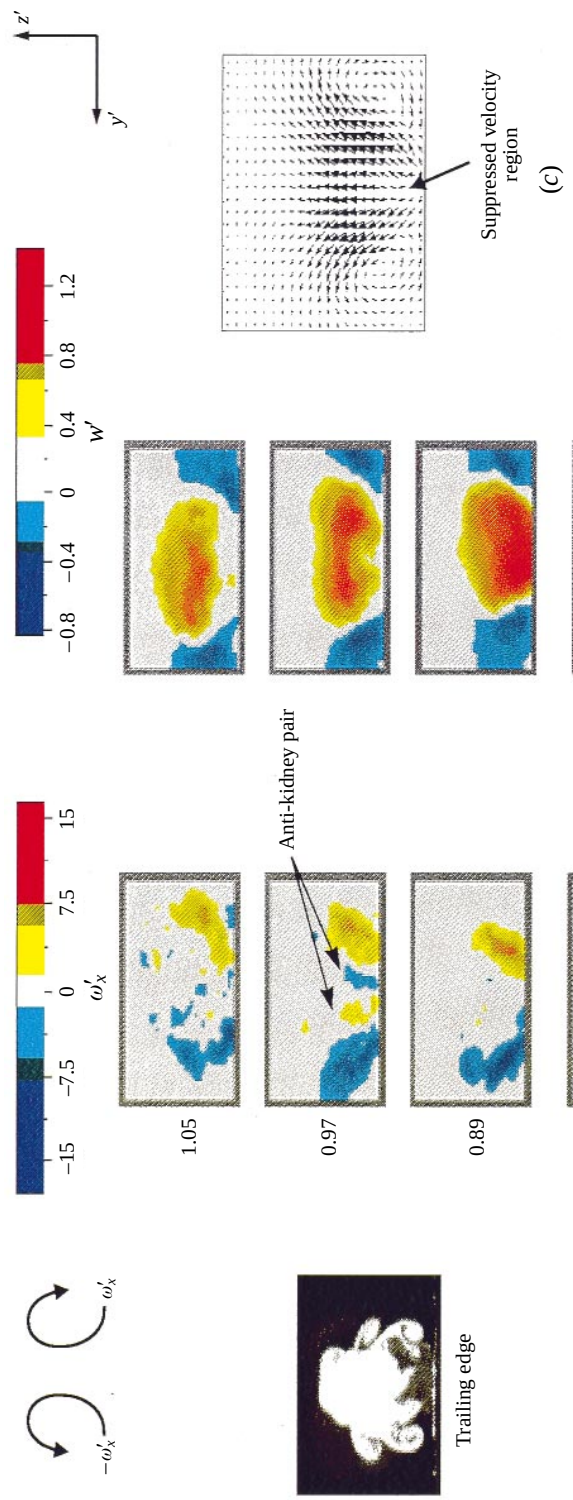

FIGURE 30. Time-averaged plots for the round hole (hole 3) at $VR = 1.6$: (*a*) vorticity, (*b*) w'-velocity, (*c*) vector plot at $x' = 0.97$. The view is from upstream.

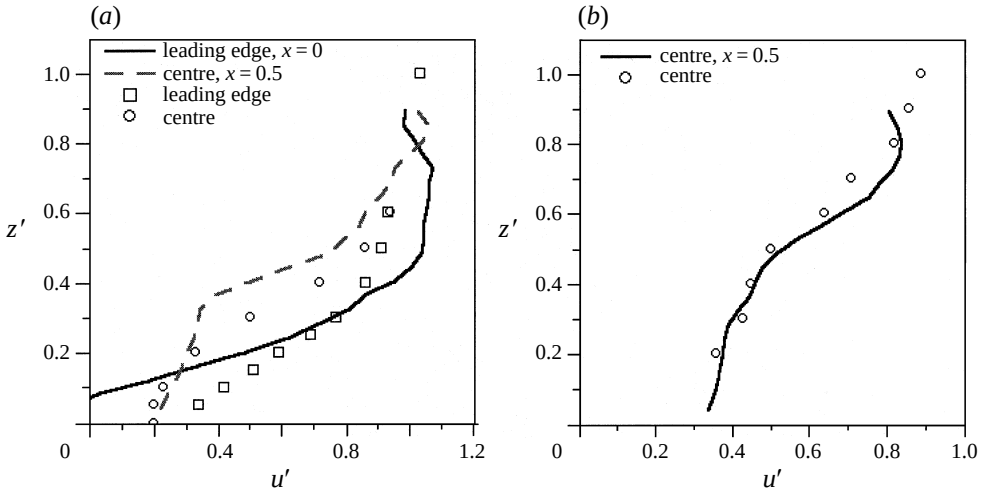

FIGURE 31. Time-averaged u'-velocity profiles at the leading edge and hole centre along the hole centreline $y' = 0$ for a round hole (hole 3) at (*a*) $VR = 0.6$ and (*b*) $VR = 1.0$. The symbols are for data from Andreopoulos & Rodi (1984) for (*a*) $VR = 0.5$ and (*b*) $VR = 1.0$.

along the hole centreline, compare favourably with those obtained by Andreopoulos & Rodi (1984, figures 5*a* and 6 for $VR = 0.5$ and 1.0).

Regardless of the blowing ratios, the magnitude of the non-dimensional vorticity, scaled by U_j, is measured to be comparable (Haven, 1996). This is consistent with the results of Fearn & Weston (1974), who found that the initial strength of the vortex pair is directly proportional to the jet velocity. This proportional relationship is also true for the other holes.

As with all the holes, the w'-velocity at the leading edge, shown in figure 30(*b*) at $x' = 0.0$, is in the negative z-direction. This negative velocity induced by the horseshoe vortex and the leading edge vortices is observable in figure 2(*b*) of Fric & Roshko (1994) and described explicitly in Kelso *et al.* (1996). It also explains the reason for the reduced values of C_p measured on the wall near the leading edge, around 0.5 to 0.7 (e.g. Fearn & Weston 1975; Sugiyama 1995).

The lateral spillage and roll-up (§5.1) are shown again for a round hole as a vector plot in the (y, z)-plane in figure 32(*a*). This is reminiscent of what is called by Kelso *et al.* (1996) the 'hovering vortex'. In addition to the lateral spillage, the crossflow also forces the jet fluid to turn again around the hole, which can be seen in the vector plot in the (x, y)-plane, figure 32(*b*). The dual acceleration associated with both the lateral spillage and turning of the jet around the hole appears to be the explanation for the previously reported results showing that the static pressure around the sides of a round jet to be substantially lower. For instance, Sugiyama's (1995) results for the pressure coefficient along the circumference show that at $VR = 1.96$, its lowest value is located at the side of the hole (90° from the leading edge) and is equal to -4.4. Interestingly, this is lower than that of the potential flow around a two-dimensional cylinder, which is -3.

As is the case for the previous holes, the vorticity along the sidewalls of the hole is lifted up as a result of the skewing of the vertical velocity at the exit plane of the hole. The w'-velocity profiles at the exit plane, shown in figure 33, agree in general with the data obtained by Crabb *et al.* (1981) and Andreopoulos (1982). Their data,

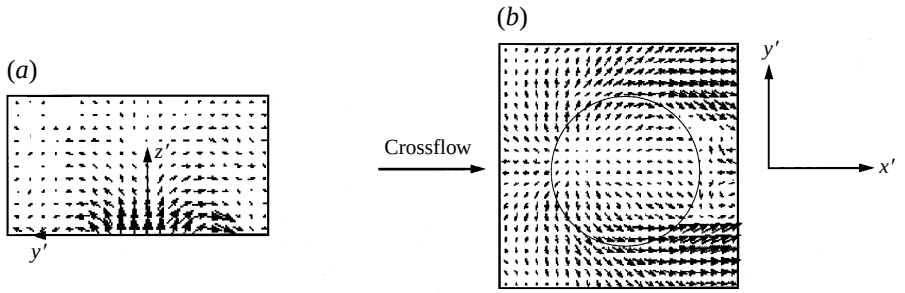

FIGURE 32. Time-averaged vector plots for a round hole (hole 3) at $VR = 0.8$: (*a*) side spillage at $x' = 0.4$, (*b*) lateral and streamwise spillage at $z' = 0$.

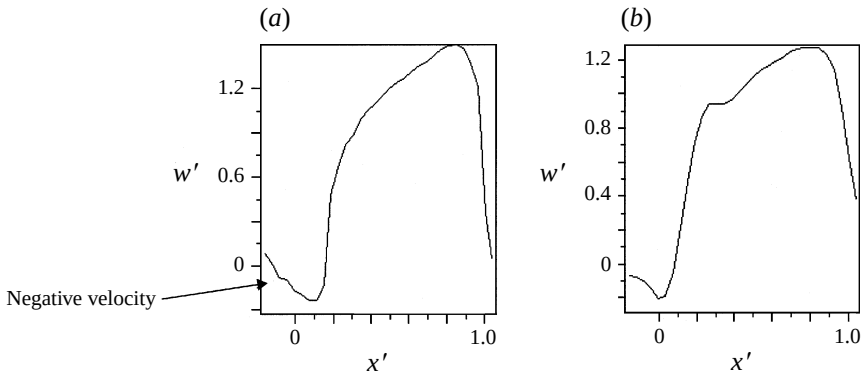

FIGURE 33. Time-averaged w'-velocity profile along the hole centreline for a round hole (hole 3): (*a*) $VR = 1.0$, (*b*) $VR = 1.6$.

however, do not show the negative velocity (except for one data point in figure 1(*a*) of Crabb *et al.*). The downstream increase of w, or skewness, observable at the exit plane implies, as pointed out by Andreopoulos (1982), that the streamlines of the jet in the (x, z)-plane start to bend well within the hole passage. The tilting of the sidewall vorticity induced by this skewness is called as the 'jet fold' by Kelso *et al.* (1996), who pointed out its connection with the kidney pair. The reverse flow at the trailing edge, shown in the u'-velocity distribution of figure 27(*c*) was observed by many studies on a round hole. The presence of the reverse flow at the leading edge may also be found in figure 5 of Andreopoulos (1982). The corner vortices at the trailing edge are sketched in figure 9 of Kelso *et al.* (1996).

9. Conclusions

At the beginning we posed two questions regarding the problem of hole geometry and jet lift-off. In specific response to these, here we summarize the results.

Question 1: Can the hole geometry alone influence lift-off? Hole geometry has a powerful influence on the very near field character of the kidney vortices. The proximity of these counter-rotating vortices relative to one another affects both the lift-off of the jet and the entrainment of crossflow fluid toward the plate surface. The results for six basic hole geometries show that the jet from the high-aspect-ratio holes, with increased separation distance between the sidewall vortices, stays attached to the surface even for higher blowing ratios, while for the low-aspect-ratio holes,

it tends to blow off (figures 4, 5, and 6). Thus, by manipulating the hole geometry alone, without increasing the hole cross-sectional area, one can reduce jet lift-off. We add, however, that although the width of the sidewall fixes the separation distance between the sidewall vortices, the other walls of the hole also modify the vortical structures significantly, as recapitulated below.

Question 2: Do the leading- and trailing-edge boundary layers simply cancel each other, or do they modify the effect of the sidewall boundary layer to influence jet lift-off? The flow visualization and PIV reveal distinct contributions to the kidney-vortices from the leading- and trailing-edge boundary layers. The use of non-circular geometries enables us to draw the clear distinction between the vorticity arising from the leading and trailing edges and that from the sidewall boundary layer.

The outer portion of the leading-edge boundary layer spills out sideways upon leaving the hole and then combines with the sidewall boundary layer, forming the steady lower deck of kidney vortical structure. The central portion of the leading-edge boundary layer is periodically shed from the hole and rides on top of the jet. The periodic vortex shows in the jet cross-sections as either an unsteady kidney or an anti-kidney vortex pair on top of the steady lower-deck vortices. The hole geometry determines how the leading-edge boundary layer is warped to induce this unsteady kidney or anti-kidney pair: the unsteady kidney pair corresponds to the low-aspect-ratio hole as well as square and round holes, the anti-kidney pair to the high-aspect-ratio hole (figures 4, 8, 9, 10 and 20). The magnitude of these unsteady pairs is comparable with that of the steady lower-deck vortices.

The trailing-edge boundary layer may be warped by the reverse flow, in a similar manner to the leading-edge boundary layer. The appearance of the anti-kidney pair at the trailing edge also depends on the hole geometry, just like the one at the leading edge.

Thus, in the present range of the blowing ratio, less than 2, all vorticity around the circumference of the jet influences, in one way or another, the downstream kidney-vortex structures. The flow field at a point is inseparably dependent on that at the other points.

In sum, the key results of the present study are that (*a*) hole-width fixes the separation distance between the kidney vortices, (*b*) the double-decked structures of streamwise vortices and (*c*) certain hole shapes are conducive to the formation of an anti-kidney pair of vortices in the upper deck. This anti-kidney pair competes with the kidney-vortices and the net balance between them determines jet lift-off.

The effect of an anti-kidney pair synthetically created by vortex generators upon the lift-off is demonstrated by Haven & Kurosaka (1996). The evaluation of industrial film cooling holes in the light of kidney and anti-kidney pairs are available in Haven (1996) and Haven *et al.* (1997).

The authors wish to express their gratitude to Professor R. E. Breidenthal Jr., University of Washington, Mr D. M. Kercher, General Electric Company, and Dr R. B. Rivir, Wright-Patterson Air Force Base, and anonymous referees for their helpful comments. We also appreciate the help rendered by Mr Roland Fuke, Lt Tony Simpson, and Ms Denise Yamagata.

The financial support by Air Force Office of Scientific Research under grant number F49620-95-1-0273 is greatly appreciated.

REFERENCES

Ajersch, P., Zhou, J. M., Ketler, S., Salcudean, M. & Gartshore, I. S. 1995 *ASME paper* 95-GT-9.

Andreopoulos, J. 1982 *Trans. ASME* : *J. Fluids Engng* **104**, 493–499.

Andreopoulos, J. & Rodi, W. 1984 *J. Fluid Mech.* **138**, 93–127.

Broadwell, J. E. & Breidenthal, R. E. 1984 *J. Fluid Mech.* **148**, 405–412.

Crabb, D., Durao, D. F. G. & Whitelaw, J. H. 1981 *Trans. ASME* : *J. Fluids Engng* **103**, 142–153.

Fearn, R. L. & Weston, R. P. 1974 *AIAA J.* **12** 1666–1671.

Fearn, R. L. & Weston, R. P. 1975 *NASA TN* D-7916.

Fric, T. F. 1990 Structure in the near field of the transverse jet. PhD thesis, Cal Tech.

Fric, T. F. & Roshko, A. 1994 *J. Fluid Mech.* **279**, 1–47.

Hagen, J. P. & Kurosaka, M. 1993 *Phys. Fluids* A **5**, 3167–3174.

Haven, B. A. 1996 The effect of hole geometry on the near field character of crossflow jets. PhD thesis, Department of Aeronautics and Astronautics, University of Washington.

Haven, B. A & Kurosaka, M. 1996 *AIAA J.* **34**, 2443–2444.

Haven, B. A, Yamagata, D. K, Kurosaka, M., Yamawaki, S. & Maya, T. 1997 *ASME Paper* 97-GT-45.

Hoult, D. P. & Weil, J. C. 1972 *Atmos. Envir.* **6**, 513–531.

Kelso, R. M., Lim, T. T. & Perry, A. E. 1996 *J. Fluid Mech.* **306**, 111–144.

Kelso, R. M., Lim, T. T. & Perry, A. E. 1997 *Phys. Fluids*, to appear.

Kurosaka, M., Christiansen, W. H., Goodman, J. R., Tirres, L. & Wohlman, R. A. 1988 *AIAA J.* **26**, 1403–1405.

Liscinsky, D. S., True, B. & Holdeman, J. D. 1995 *AIAA Paper* 95-0732.

Moore, D. W. 1976 *Mathematica* **23**, 35–44.

Moussa, Z. M., Trischka, J. W. & Eskinazi, S. 1977 *J. Fluid Mech.* **80**, 49–80.

Saffman, P. G. & Baker, G. R. 1979 *Ann. Rev. Fluid Mech.* **11**, 100.

Scorer, R. S. 1958 *Natural Aerodynamics*, pp. 194, 210. Pergamon.

Sugiyama, Y. 1995 *International Gas Turbine Congress, Yokohama.* vol. II pp. 375–382.

Sykes, R. I., Lewellen, W. S. & Parker, S. F. 1986 *J. Fluid Mech.* **168**, 393–413.

Wu, J. M., Vakili, A. D. & Yu, F. M. 1988 *AIAA J.* **26**, 940–947.